

---

# GRADIENT ALIGNMENT IN PHYSICS-INFORMED NEURAL NETWORKS: A SECOND-ORDER OPTIMIZATION PERSPECTIVE

---

Sifan Wang<sup>1,\*</sup>, Ananya Kumar Bhartari<sup>2,\*</sup>, Bowen Li<sup>3,\*</sup>, Paris Perdikaris<sup>2</sup>

<sup>1</sup>Institution for Foundation of Data Science, Yale University

<sup>2</sup>Department of Mechanical Engineering and Applied Mechanics, University of Pennsylvania

<sup>3</sup>Department of Mathematics, City University of Hong Kong

sifan.wang@yale.edu, ananya@seas.upenn.edu, bowen.li@cityu.edu.hk, pgp@seas.upenn.edu

## ABSTRACT

Multi-task learning through composite loss functions is fundamental to modern deep learning, yet optimizing competing objectives remains challenging. We present new theoretical and practical approaches for addressing directional conflicts between loss terms, demonstrating their effectiveness in physics-informed neural networks (PINNs) where such conflicts are particularly challenging to resolve. Through theoretical analysis, we demonstrate how these conflicts limit first-order methods and show that second-order optimization naturally resolves them through implicit gradient alignment. We prove that SOAP, a recently proposed quasi-Newton method, efficiently approximates the Hessian preconditioner, enabling breakthrough performance in PINNs: state-of-the-art results on 10 challenging PDE benchmarks, including the first successful application to turbulent flows with Reynolds numbers up to 10,000, with 2-10x accuracy improvements over existing methods. We also introduce a novel gradient alignment score that generalizes cosine similarity to multiple gradients, providing a practical tool for analyzing optimization dynamics. Our findings establish frameworks for understanding and resolving gradient conflicts, with broad implications for optimization beyond scientific computing.

## 1 Introduction

Multi-task learning through composite loss functions has become a cornerstone of modern deep learning, from computer vision to scientific computing. However, when different loss terms compete for model capacity, they can generate conflicting gradients that impede optimization and degrade performance. While this fundamental challenge is known to the multi-task learning literature [1–3], several challenges remain open, particularly in settings where objectives are tightly coupled through complex physical constraints.

In this work, we examine gradient conflicts through the lens of physics-informed neural networks (PINNs), where the challenge manifests acutely due to the inherent coupling between physical constraints and data-fitting objectives. Our key insight is that while first-order optimization methods struggle with competing objectives, appropriate preconditioning can naturally align gradients to enable efficient optimization. While our findings on gradient alignment and second-order preconditioning have broad implications for multi-task learning, here we focus on PINNs as they provide an ideal testbed: their physically-constrained objectives are mathematically precise, their solutions can be rigorously verified, and their performance bottlenecks are well-documented. Through theoretical analysis and extensive experiments on challenging partial differential equations (PDEs), we demonstrate breakthrough results in problems ranging from basic wave propagation to turbulent flows.

To better motivate our approach, consider training a PINN to solve the Navier-Stokes equations. The model must simultaneously satisfy boundary conditions, conservation laws, and empirical measurements – objectives that often push a neural network’s parameters in opposing directions. Traditional methods like Adam or gradient descent struggle

---

\* These authors contributed equally to this work.

as they can only follow the average gradient direction, leading to slow convergence or poor solutions. In contrast, second-order methods can identify and resolve these conflicts through implicit gradient alignment, enabling more efficient optimization. To this end, the key contributions of this work are:

- A novel gradient alignment metric that extends cosine similarity to quantify directional conflicts between multiple loss terms, providing a systematic tool for analyzing multi-task optimization dynamics.
- Systematic analysis demonstrating that gradient conflicts are a fundamental barrier in PINNs training, with quantitative evidence linking higher conflict scores to slower convergence across diverse PDE systems.
- Theoretical characterization of how different optimizers handle gradient conflicts, proving that second-order methods inherently promote gradient alignment through implicit preconditioning of the loss landscape.
- Analysis showing that SOAP [4], a scalable quasi-Newton method, provides an efficient approximation to the optimal Newton preconditioner while remaining computationally tractable, explaining its effectiveness in resolving gradient conflicts.
- Breakthrough experimental results across 10 challenging PDE benchmarks, including the first successful application of PINNs to turbulent flows with Reynolds numbers up to 10,000, achieving 2-10x improvement in accuracy over existing methods.

Taken together, this work advances our understanding of optimization dynamics in PINNs while demonstrating how quasi second-order methods can enable more reliable neural PDE solvers for solving complex physical systems. These insights pave the way for developing next-generation optimizers for physics-informed machine learning, and beyond.

## 2 Problem Formulation

**Overview.** Multi-task learning in deep neural networks requires simultaneously minimizing multiple competing objectives – a challenge that manifests acutely in physics-informed neural networks (PINNs). Building upon the work of [5], PINNs approximate solutions to partial differential equations by minimizing a composite loss function that enforces both physical constraints and data-fitting objectives. Consider a general PDE system:

$$\mathbf{u}_t + \mathcal{N}[\mathbf{u}] = 0, \quad t \in [0, T], \quad \mathbf{x} \in \Omega, \quad (2.1)$$

with initial and boundary conditions

$$\mathbf{u}(0, \mathbf{x}) = \mathbf{g}(\mathbf{x}), \quad \mathbf{x} \in \Omega, \quad (2.2)$$

$$\mathcal{B}[\mathbf{u}] = 0, \quad t \in [0, T], \quad \mathbf{x} \in \partial\Omega, \quad (2.3)$$

where  $\mathcal{N}[\cdot]$  represents a differential operator and  $\mathcal{B}[\cdot]$  denotes boundary conditions. The core idea of PINNs is to approximate the solution  $\mathbf{u}(t, \mathbf{x})$  using a neural network  $\mathbf{u}_\theta(t, \mathbf{x})$ . Through automatic differentiation [6], we can compute the PDE residual:

$$\mathcal{R}[u_\theta](t, \mathbf{x}) = \frac{\partial \mathbf{u}_\theta}{\partial t}(t_r, \mathbf{x}_r) + \mathcal{N}[\mathbf{u}_\theta](t_r, \mathbf{x}_r). \quad (2.4)$$

This leads to a composite loss function that encapsulates multiple competing objectives:

$$\mathcal{L}(\theta) = \underbrace{\frac{1}{N_{ic}} \sum_{i=1}^{N_{ic}} |\mathbf{u}_\theta(0, \mathbf{x}_{ic}^i) - \mathbf{g}(\mathbf{x}_{ic}^i)|^2}_{\mathcal{L}_{ic}(\theta)} + \underbrace{\frac{1}{N_{bc}} \sum_{i=1}^{N_{bc}} |\mathcal{B}[\mathbf{u}_\theta](t_{bc}^i, \mathbf{x}_{bc}^i)|^2}_{\mathcal{L}_{bc}(\theta)} + \underbrace{\frac{1}{N_r} \sum_{i=1}^{N_r} |\mathcal{R}[\mathbf{u}_\theta](t_r^i, \mathbf{x}_r^i)|^2}_{\mathcal{L}_r(\theta)}. \quad (2.5)$$

These loss functions aim to fit the initial, boundary conditions and the PDE residuals, respectively. And  $\{\mathbf{x}_{ic}^i\}_{i=1}^{N_{ic}}$ ,  $\{t_{bc}^i, \mathbf{x}_{bc}^i\}_{i=1}^{N_{bc}}$  and  $\{t_r^i, \mathbf{x}_r^i\}_{i=1}^{N_r}$  may be selected either as fixed mesh vertices or through random sampling during each training iteration.

Here lies the fundamental challenge: these different loss terms frequently work against each other during optimization. Consider the Navier-Stokes equations – enforcing no-slip boundary conditions requires precise control of velocity gradients near walls, which can conflict with maintaining conservation of mass and momentum in the bulk flow. When such conflicts occur, first-order methods like gradient descent or Adam can only follow the average gradient direction, leading to inefficient optimization trajectories that zigzag between competing objectives. The severity of these conflicts increases with problem complexity, becoming particularly acute for turbulent flows where maintaining physical constraints across multiple scales is crucial.

**Main Idea.** Here we resolve these challenges following three key steps. First, we develop a gradient alignment score that quantifies conflicts between different loss terms, providing a systematic way to analyze optimization dynamics. Second, we prove that second-order optimization methods can naturally resolve these conflicts through implicit gradient alignment via preconditioned updates. Finally, we demonstrate that SOAP [4] offers an elegant and computationally tractable approximation to the optimal preconditioner, enabling breakthrough performance on challenging PDEs including turbulent flows.

### 3 Methods

**Gradient Alignment in PINNs.** PINNs face a fundamental challenge of competing gradients during training, which manifests in two distinct modes, see Figure 1. The first mode, identified by [7, 8], involves back-propagated gradients of significantly different magnitudes. When these magnitude imbalances occur, certain loss terms dominate the optimization process, leading to model failure. While this challenge has been partially addressed through self-adaptive weighting schemes [9–13], a second, more fundamental mode of gradient conflict remains less explored.

This second mode occurs when gradients from different loss terms point in opposing directions, forcing the optimization to follow inefficient trajectories. Traditional scaling-based approaches cannot resolve these directional conflicts, which become particularly severe in complex PDE systems where multiple physical constraints must be simultaneously satisfied. To systematically study and address this challenge, here we introduce a new metric called the *alignment score*, defined as follows.

**Definition 1.** Suppose that  $v_1, v_2, \dots, v_n$  are vectors, then the alignment score is defined as

$$\mathcal{A}(v_1, v_2, \dots, v_n) = 2 \left\| \frac{\sum_{i=1}^n \frac{v_i}{\|v_i\|}}{n} \right\|^2 - 1. \quad (3.1)$$

This score ranges from  $[-1, 1]$  and naturally extends the concept of cosine similarity to multiple vectors. As illustrated in Proposition 1, for the special case of  $n = 2$ , our score exactly recovers the standard cosine similarity  $\cos(v_1, v_2) = \frac{v_1 \cdot v_2}{\|v_1\| \|v_2\|}$ , where 1 indicates perfect alignment, 0 suggests orthogonal directions, and -1 represents complete opposition.

**Proposition 1.** For  $n=2$ , the alignment score  $\mathcal{A}(v_1, v_2)$  equals the cosine similarity between  $v_1$  and  $v_2$ :

$$\mathcal{A}(v_1, v_2) = \cos(v_1, v_2) = \frac{v_1 \cdot v_2}{\|v_1\| \|v_2\|}. \quad (3.2)$$

The proof is provided in Appendix E.1. The alignment score enables us to quantify both the local conflicts between individual loss terms within each gradient descent step and the global conflicts across consecutive steps. Formally:

**Definition 2.** Let  $\mathcal{L} = \sum_{i=1}^n \mathcal{L}_i$  be a composite loss function. At the  $k$ -th step of gradient descent, let  $g^k$  denote the full gradient and  $g_1^k, g_2^k, \dots, g_n^k$  denote the gradients of individual loss terms. We define:

(a) The intra-step gradient alignment score:

$$\mathcal{A}_{intra}^k = \mathcal{A}(g_1^k, g_2^k, \dots, g_n^k). \quad (3.3)$$

(b) The inter-step gradient alignment score:

$$\mathcal{A}_{inter}^k = \mathcal{A}(g^{k-1}, g^k). \quad (3.4)$$

In the following, we will demonstrate that gradient direction conflicts widely exist in training PINNs, especially in the early stages of training. To this end, we conduct experiments on five representative PDEs spanning from linear

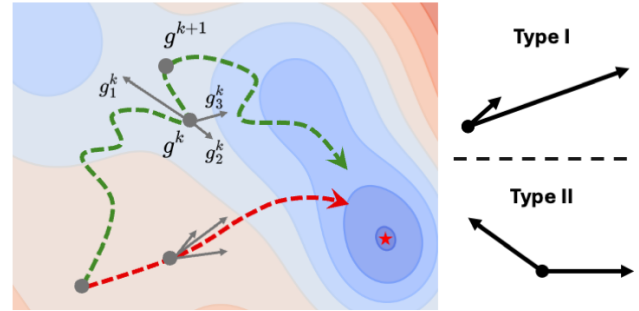


Figure 1: Gradient conflicts and their impact on PINNs optimization. The irregular green trajectory illustrates how the optimization struggles when facing two types of gradient conflicts: Type I, where gradients have similar directions but vastly different magnitudes, and Type II, where gradients have similar magnitudes but opposing directions. The red trajectory shows how appropriate preconditioning through second-order information could mitigate these conflicts by aligning gradients both within and between optimization steps, enabling efficient convergence.

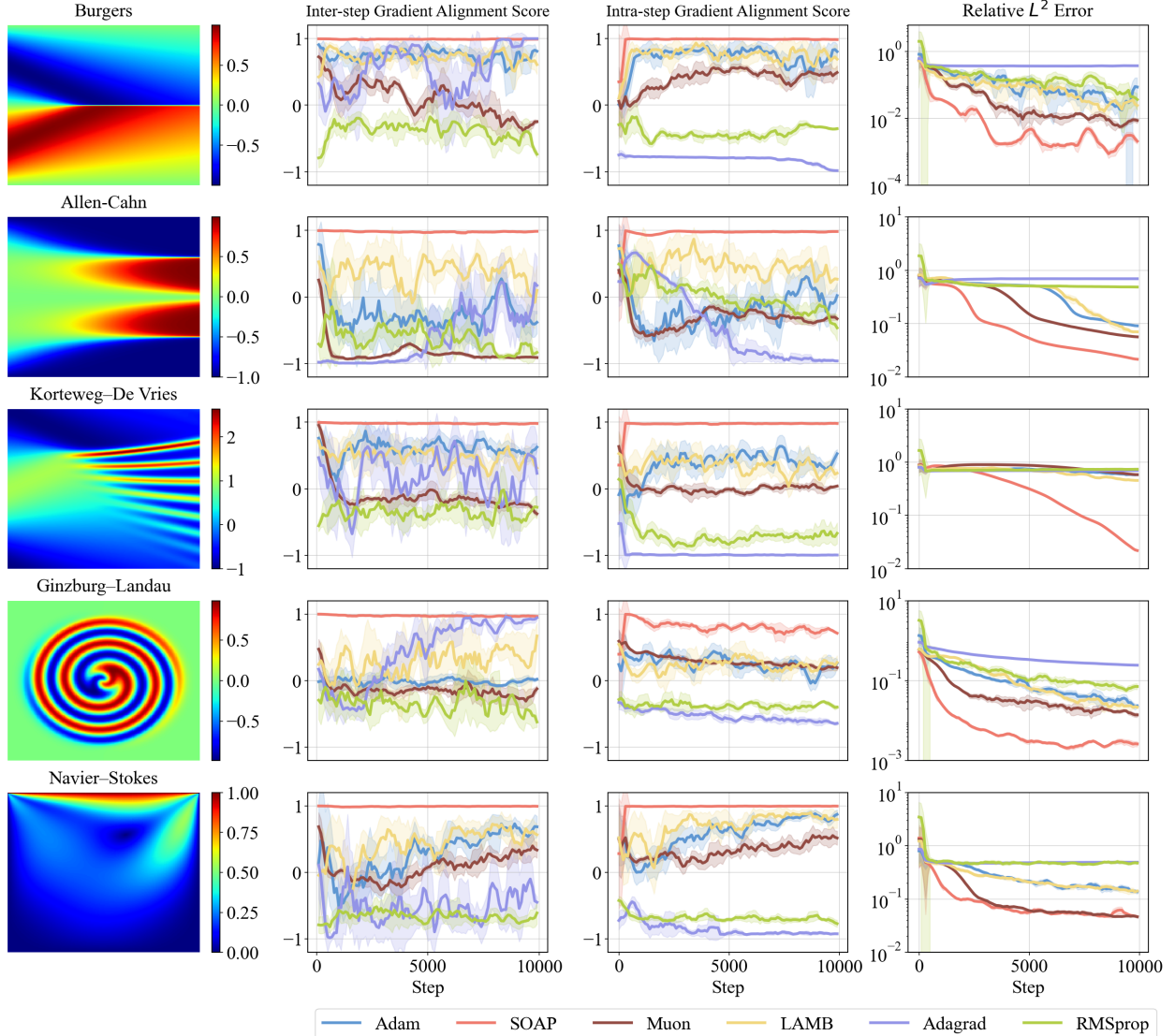


Figure 2: Gradient alignment scores and test errors obtained by training PINNs with different optimizers across different PDEs. From left to right: ground truth PDE solution, intra-step gradient alignment scores (Eq. (3.3)), inter-step gradient alignment scores (Eq. (3.4)), and test error convergence during training.

wave propagation to reaction-diffusion systems like the Ginzburg-Landau equation and fluid dynamics governed by the Navier-Stokes equations. The detailed experimental setup is provided in Appendix F.

Figure 2 visualizes the evolution of inter-step and intra-step gradient alignment scores alongside the error convergence during training with different common optimizers. In all cases except SOAP, we observe that both scores oscillate significantly near or below zero, providing strong evidence for persistent directional conflicts between gradients throughout the training process. Intuitively, these conflicting gradients force the network parameters to follow an inefficient zigzag trajectory in the loss landscape, significantly impeding convergence speed.

In contrast, the SOAP optimizer consistently maintains the highest positive values for both inter-step and intra-step gradient alignment scores throughout training. This effective resolution of gradient direction conflicts directly corresponds to significantly faster convergence in test error.

The following section analyzes SOAP’s theoretical foundations, focusing on two critical aspects that illuminate the gradient conflict problem in PINNs. We first demonstrate why conventional first-order optimizers fundamentally struggle with directional conflicts, then show how SOAP’s second-order preconditioning naturally resolves these challenges. For ease of exposition, all the proofs supporting this analysis can be found in Appendices C and D.

**Inter-step Gradient Alignment.** Having preliminarily demonstrated SOAP’s empirical effectiveness, we now analyze its mechanism through the lens of second-order optimization. Given the model parameters  $\theta_t \in \mathbb{R}^p$  at iteration  $t$ , and the gradient  $g_t \in \mathbb{R}^p$  of the loss function with respect to  $\theta_t$ , the Newton update is  $\theta_{t+1} = \theta_t - H^{-1}g_t$ , where  $H \in \mathbb{R}^{p \times p}$  is the Hessian matrix of the loss function, providing a preconditioner that scales the gradient by the local curvature information to achieve faster convergence than first-order methods. By the following lemma, we point out that second-order methods, through their preconditioning matrices, naturally induce positive inter-gradient alignment.

**Lemma 1.** *Let  $\mathcal{L}(\theta) : \mathbb{R}^p \rightarrow \mathbb{R}$  be a twice differentiable loss function with Hessian  $H(\theta)$ . Assume that the inverse of Hessian is uniformly bounded. For the Newton iteration with a learning rate  $\eta > 0$ :*

$$\theta_{t+1} = \theta_t - \eta H^{-1}(\theta_t)g_t, \quad (3.5)$$

with  $g_t$  being the gradient at  $\theta_t$ , the inter-step gradient alignment score satisfies

$$\mathcal{A}(g_t, g_{t+1}) = 1 + O(\eta^2 \|g_t\|). \quad (3.6)$$

For sufficiently small learning rates, Lemma 1 shows that Hessian preconditioning naturally promotes gradient alignment across optimization steps. This theoretical result aligns with our empirical observations of SOAP’s behavior in Figure 2, suggesting a deeper connection between SOAP and Newton’s method that we will explore in subsequent sections.

Recent work on practical second-order optimization has focused on developing efficient preconditioners for large neural networks trained with mini-batches. Adagrad [14] introduced the fundamental idea of using accumulated gradient covariance as a preconditioner  $H_{\text{Ada}} = \sum_{s=1}^t g_s g_s^\top$ , leading to the update rule:

$$\theta_{t+1} = \theta_t - \eta H_{\text{Ada}}^{-1/2} g_t. \quad (3.7)$$

This approach has theoretical connections to the Hessian matrix [14, 15] and has inspired several extensions including K-FAC [16], GGT [17], and Shampoo [18].

Shampoo [18] further develops this idea by approximating  $H_{\text{Ada}}$  through Kronecker factorization. For a layer with weight matrix  $W_t$  and gradient  $G_t \in \mathbb{R}^{m \times n}$ , Shampoo maintains two preconditioners:

$$\begin{aligned} L_t &= L_{t-1} + G_t G_t^\top \in \mathbb{R}^{m \times m}, \\ R_t &= R_{t-1} + G_t^\top G_t \in \mathbb{R}^{n \times n}, \end{aligned}$$

initialized as  $\epsilon I_m$  and  $\epsilon I_n$ . The weight update then becomes:

$$W_{t+1} = W_t - \eta L_t^{-1/4} G_t R_t^{-1/4}. \quad (3.8)$$

This formulation not only approximates the full Adagrad preconditioner [19, 20], but also provides a Kronecker product approximation to the Gauss-Newton component of the layerwise Hessian [20] (see Remark 1). This connection to second-order information will prove crucial for understanding SOAP’s effectiveness.

**SOAP for PINNs.** Before diving into the formal analysis, let us build some intuition for why SOAP is particularly effective at resolving gradient conflicts. The key insight comes from understanding how second-order information captures interactions between different loss terms. When gradients conflict, it typically indicates that improving one objective requires coordinated changes across multiple parameters – information that is encoded in the Hessian matrix’s off-diagonal elements.

SOAP approximates this second-order information in two complementary ways: (i) Its block-diagonal structure naturally captures parameter interactions within each network layer; (ii) Its adaptive preconditioner accumulates information about gradient correlations across training steps. This allows SOAP to implicitly identify and exploit parameter update directions that simultaneously improve multiple objectives. Rather than simply following the average gradient, SOAP can utilize the local loss landscape geometry to find more direct paths to good solutions. The following sections make this intuition precise through formal analysis of SOAP’s convergence properties and gradient alignment characteristics.

We now show that SOAP can be interpreted as an approximation to Newton’s method, providing theoretical justification for the high inter-step gradient alignment observed in Figure 2. The key insight comes from analyzing how SOAP modifies Shampoo’s preconditioner structure.

SOAP [4] enhances Shampoo’s efficiency by performing optimization in a transformed space aligned with the preconditioner’s principal directions. For each layer’s weight matrix and gradient  $G_t \in \mathbb{R}^{m \times n}$ , SOAP maintains two covariance matrices using exponential moving averages:

$$L_t = \beta_2 L_{t-1} + (1 - \beta_2) G_t G_t^\top, \quad (3.9)$$

$$R_t = \beta_2 R_{t-1} + (1 - \beta_2) G_t^\top G_t. \quad (3.10)$$

These matrices are then eigendecomposed as  $L_t = Q_L \Lambda_L Q_L^T$  and  $R_t = Q_R \Lambda_R Q_R^T$ , where  $\Lambda_L$  and  $\Lambda_R$  contain the eigenvalues that capture the principal curvature directions of the loss landscape.

At each iteration  $t$ , SOAP updates each layer’s weight matrix  $W_t$  using its corresponding gradient  $G_t$  as follows:

1. Project the gradient into the eigenspace: 
$$\tilde{G}_t = Q_L^T G_t Q_R.$$
2. Apply the Adam update in the *rotated* space: 
$$\widetilde{W}_{t+1} = \widetilde{W}_t - \eta \text{Adam}(\tilde{G}_t).$$
3. Transform back to the original parameter space: 
$$W_{t+1} = Q_L \widetilde{W}_{t+1} Q_R^T.$$

To reduce computational overhead, the preconditioners  $L_t$  and  $R_t$  are updated with frequency  $f$  in practice. We will analyze the impact of update frequency and momentum parameters through ablation studies in Section 4.

To establish SOAP’s connection to Newton’s method, we begin by examining how the Hessian matrix can be approximated in neural networks. For networks trained with cross-entropy loss, the Gauss-Newton approximation takes the form:

$$H_{\text{GN}} = \mathbb{E} \left[ \frac{\partial f}{\partial W} \frac{\partial^2 \mathcal{L}}{\partial f^2} \frac{\partial f^T}{\partial W} \right] = \mathbb{E} [g g^T], \quad (3.11)$$

where  $\mathcal{L}$  denotes the loss function,  $f$  represents network outputs, and  $G = \frac{\partial \mathcal{L}}{\partial W}$  is the gradient matrix with vectorization  $g = \text{vec}(G)$ . Empirical evidence from [21] supports a key simplifying assumption:

**Assumption 1.** *The Gauss-Newton component provides a good approximation to the true Hessian:  $H_{\text{GN}} \approx H$ .*

This approximation leads to our main theoretical result connecting SOAP to Newton’s method:

**Theorem 1.** *Under Assumption 1 and the conditions of Proposition 4, SOAP’s update approximates Newton’s method:*

$$w_{t+1} = w_t - \eta \text{Soap}(g_t) \approx w_t - \eta H^{-1} g_t. \quad (3.12)$$

The complete proof is provided in Appendix C. The key insight is that SOAP effectively approximates the block-diagonal Hessian in a rotated space, with each block corresponding to a layer-wise Kronecker factorization. This structure naturally promotes gradient alignment across optimization steps, as we demonstrated theoretically in Lemma 1 and observed empirically in Figure 2.

**Remark 1.** *While SOAP effectively approximates Newton’s method through its block-diagonal structure, other optimizers make different compromises in their approximations. Adam can approximate Newton’s method, but requires the highly restrictive assumption that the Hessian matrix is diagonal. Similarly, Shampoo takes a different approach by using the square root of the Gauss-Newton component as its preconditioner [20]:*

$$\text{Shampoo}(g_t) \approx H_{\text{GN}}^{-1/2} g_t \approx H^{-1/2} g_t. \quad (3.13)$$

These structural differences help explain why SOAP achieves better gradient alignment than both Adam and Shampoo.

In the following proposition we show that SOAP’s approximation of Newton’s method enables it to resolve such conflicts during training. The proof can be found in Appendix E.3. Note that this result is general, not limited to types of PDEs and network architectures, and can be extended to other multi-task learning problems in principle.

**Proposition 2.** *Assume that there exists a global minima  $\theta^* \in \mathbb{R}^p$  corresponding to the true PDE solution such that  $\mathcal{L}_{ic}(\theta^*) = \mathcal{L}_{bc}(\theta^*) = \mathcal{L}_r(\theta^*) = 0$ . When applying SOAP optimizers to  $\mathcal{L}_{ic}$ ,  $\mathcal{L}_{bc}$  and  $\mathcal{L}_r$  separately, for each weight matrix  $W$  we have*

$$\lim_{\theta \rightarrow \theta^*} \mathcal{A}(\text{Soap}(G_{ic}), \text{Soap}(G_{bc}), \text{Soap}(G_r)) \approx 1, \quad (3.14)$$

with  $G_{ic} = \frac{\partial \mathcal{L}_{ic}}{\partial W}$ ,  $G_{bc} = \frac{\partial \mathcal{L}_{bc}}{\partial W}$  and  $G_r = \frac{\partial \mathcal{L}_r}{\partial W}$ .

**Remark 2** (Limitation of Shampoo). *An important limitation of Shampoo arises from its use of  $H^{-1/2}$  rather than  $H^{-1}$  in its approximation. This square root term prevents cancellation of the Hessian components in our theoretical analysis, making it impossible to establish gradient alignment guarantees similar to those we proved for SOAP. Our empirical investigation supports this theoretical insight. Using Muon [22], a computationally efficient variant of Shampoo, we observe that despite achieving reasonable convergence in the loss function, the optimizer maintains consistently low gradient alignment scores throughout training (Figure 2). This evidence reinforces our theoretical understanding of the Hessian approximation, as used in SOAP, is crucial for resolving gradient conflicts.*

## 4 Experiments

To rigorously evaluate SOAP’s performance, we examine a diverse set of 10 representative and challenging PDEs that govern fundamental physical phenomena. These equations span wave propagation, shock formulation, chaotic systems, reaction-diffusion processes, fluid dynamics, and heat transfer. The detailed description of the problem setup, including the PDE parameters, initial and boundary conditions, numerical implementations, and supplementary visualizations, are presented in Appendix F.

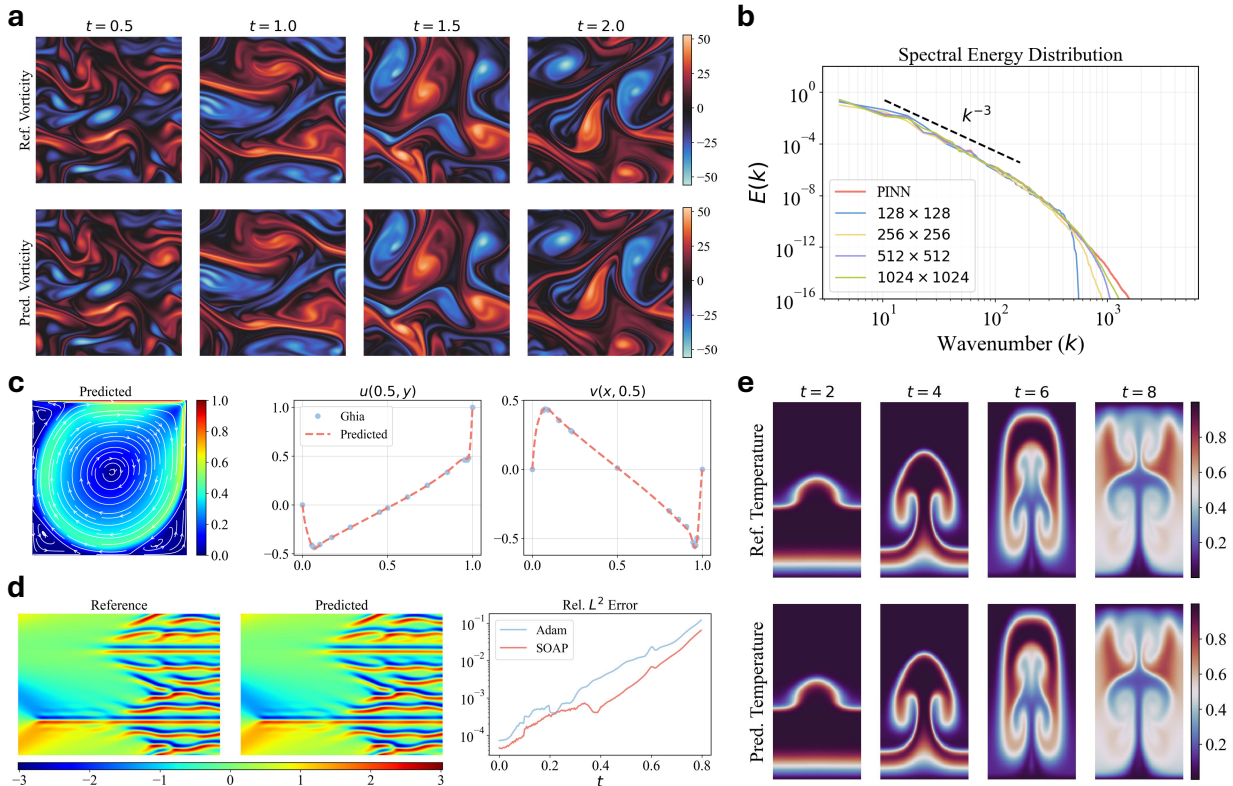


Figure 3: Simulating complex fluid dynamics using PINNs with SOAP optimization. (a) Kolmogorov flow at  $Re=10,000$ : comparison between reference solution and PINN predictions demonstrates accurate capture of turbulent structures across multiple time steps. (b) Spectral energy distribution showing PINN’s superior resolution of fine-scale dynamics compared to traditional numerical solutions at various grid resolutions. (c) Lid-driven cavity flow at  $Re=5,000$ : streamlines and centerline velocity profiles show excellent agreement with benchmark data from [23]. (d) Kuramoto-Sivashinsky equation: PINNs accurately predicts complex spatiotemporal patterns and chaotic dynamics. (e) Rayleigh-Taylor instability ( $Pr=0.71, Ra=10^6$ ): evolution of temperature field shows precise capture of interface dynamics and mushroom-shaped structures characteristic of this flow.

**Baselines.** We focus our comparisons on PINN approaches that have the potential to scale to training large neural networks, as these are promising for solving realistic large-scale physical problems in the future. That said, we do not compare against PINNs trained with natural gradients [24, 25] and L-BFGS variants [26], since these methods are limited to small networks and full-batch gradient descent, making them impractical for the challenging PDEs we consider.

Our baselines follow the current state-of-the-art training pipeline established by [27]. Unless otherwise specified, we use PirateNet [28] as the backbone architecture, with three residual blocks, a hidden dimension of 256, and Tanh activation functions. All weight matrices are enhanced using random weight factorization (RWF) [29], with  $\mu = 1.0, \sigma = 0.1$ . Exact periodic boundary conditions are strictly enforced when applicable [30].

For model training, we use mini-batch gradient descent with the Adam optimizer [31], which has become the de facto standard for training PINNs due to its robust performance and computational efficiency. We randomly sample 8,192 collocation points at each iteration. The learning rate schedule begins with a linear warm-up phase over the first 5,000 steps, increasing from 0 to 0.001, followed by an exponential decay with a factor of 0.9. To improve training

efficiency and robustness, we use learning rate annealing [7, 27] for loss balancing. The loss weights are updated every 1,000 iterations with a moving average. In addition, we employ causal training [27, 32] to address causality violations when solving time-dependent PDEs. The causal tolerance is set to 1.0. For challenging benchmarks, we implement time-marching and curriculum learning strategies [33]. Details of the aforementioned techniques and hyper-parameters are summarized in Appendix F.1 and F.2.

Table 1: Comparison of optimizer performance obtained by training PINNs with Adam and SOAP, respectively, across various PDEs, following the training pipeline described in Section 4. The evaluation metric is the relative  $L^2$  error over the entire spatial temporal domain.

Benchmark	Adam	SOAP
Wave	$5.15 \times 10^{-5}$	<b><math>8.05 \times 10^{-6}</math></b>
Burgers	$8.20 \times 10^{-5}$	<b><math>4.03 \times 10^{-5}</math></b>
Allen-Cahn	$2.24 \times 10^{-5}$	<b><math>3.48 \times 10^{-6}</math></b>
Korteweg–De Vries	$7.04 \times 10^{-4}$	<b><math>3.40 \times 10^{-4}</math></b>
Kuramoto-Sivashinsky	$7.48 \times 10^{-2}$	<b><math>3.86 \times 10^{-2}</math></b>
Grey-Scott	$3.61 \times 10^{-3}$	<b><math>1.18 \times 10^{-4}</math></b>
Ginzburg-Landau	$1.49 \times 10^{-2}$	<b><math>4.78 \times 10^{-3}</math></b>
Lid-driven cavity (Re = $5 \times 10^3$ )	$3.24 \times 10^{-1}$	<b><math>3.99 \times 10^{-2}</math></b>
Kolmogorov flow (Re = $10^4$ )	$2.04 \times 10^{-1}$	<b><math>6.99 \times 10^{-2}</math></b>
Rayleigh-Taylor instability (Pr = 0.71, Ra = $10^6$ )	$7.32 \times 10^{-2}$	<b><math>5.22 \times 10^{-3}</math></b>

**State-of-the-art results.** Table 1 demonstrates SOAP’s consistent performance improvements across diverse test cases. For the simple wave equation, SOAP achieves a 6.4x reduction in relative error compared to the baseline. For nonlinear 1D problems, our approach yields a 6.9x reduction for the Allen-Cahn equation and about 2x for both Korteweg–De Vries and Kuramoto-Sivashinsky problems. The performance gains become particularly pronounced for coupled diffusion-reaction systems. The Grey-Scott and Ginzburg-Landau equations exhibit an order of magnitude reduction in error. On challenging Navier-Stokes benchmarks, including the lid-driven cavity and Rayleigh-Taylor instability problems, SOAP demonstrates a more than 10x error reduction. We highlight and discuss these substantial improvements in detail below.

**Complex Fluid Dynamics.** Our most significant achievement is successfully applying PINNs to complex fluid dynamics problems that were previously considered beyond their capabilities. In particular, we demonstrate breakthrough results in three challenging cases that combine multiple physical constraints and have historically proven difficult for PINNs, see Figure 3.

For the lid-driven cavity flow at Reynolds number 5,000, SOAP enables a dramatic improvement in accuracy, reducing the relative  $L^2$  error from 32.4% to 3.99%. As shown in Figure 3c, our model successfully captures intricate flow features including secondary and tertiary corner vortices, showing excellent agreement with the benchmark results of [23]. This level of accuracy was previously unattainable with PINNs at such high Reynolds numbers.

The Rayleigh-Taylor instability presents an even more demanding test, requiring simultaneous handling of interface dynamics and coupled velocity-density evolution. SOAP enables accurate prediction of the characteristic mushroom-shaped structures that develop as heavier fluid penetrates into lighter fluid, achieving a relative  $L^2$  error of 0.52% – nearly an order of magnitude improvement over the best baseline’s 7.32%. Figure 3e demonstrates excellent agreement with reference solutions across multiple time steps, capturing both the initial linear growth phase and subsequent nonlinear development.

Our most impressive result comes from the turbulent Kolmogorov flow at Reynolds number 10,000 – marking the first time PINNs have successfully captured turbulent dynamics at such high Reynolds numbers. Our model achieves a relative  $L^2$  error of 6.99%, compared to 20.4% with our baseline. Figure 3a shows that our predictions accurately reproduce both the large-scale flow structures and the complex cascade of smaller eddies characteristic of turbulent flows. Moreover, spectral analysis reveals that our PINN solution maintains higher spectral energy at high wavenumbers compared to traditional numerical solvers, even those using a  $1024 \times 1024$  grid resolution. This demonstrates PINNs’

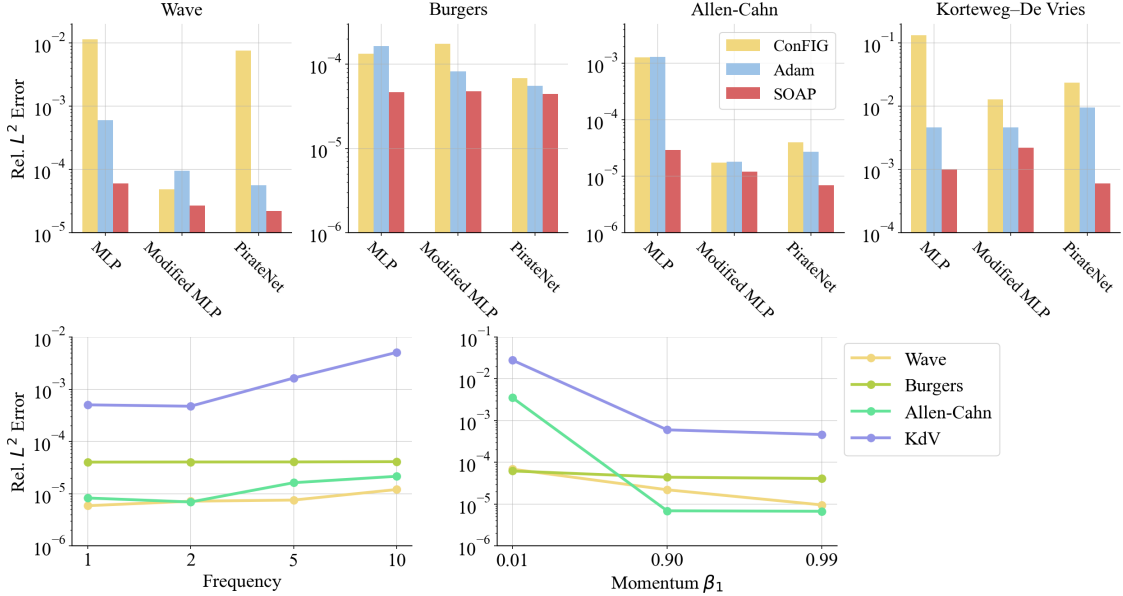


Figure 4: Optimizer performance comparison and ablation studies. Top: Relative  $L^2$  error across PDE benchmarks using different optimizers. Bottom left: Relative  $L^2$  error for varying preconditioner update frequencies in SOAP optimizer. Bottom right: Relative  $L^2$  error with different momentum values in SOAP optimizer.

potential advantage in resolving fine-scale dynamics without requiring explicit grid discretization – a key capacity for turbulence modeling.

These results represent more than just incremental improvements in accuracy. They demonstrate that PINNs, when properly optimized, can handle complex multi-physics problems previously considered beyond their capabilities. The success in these challenging cases validates our theoretical analysis showing that gradient alignment becomes increasingly critical as physical constraints become more tightly coupled.

**On the Convergence of PINNs Solutions.** An intriguing observation emerges when examining our convergence trajectories in detail. While the PINNs’ loss functions continue to decrease throughout training, indicating increasingly better satisfaction of physical and boundary constraints, the relative  $L^2$  test error against reference numerical solutions plateaus for most complex cases (notably for turbulent flows and the Rayleigh-Taylor instability, among other cases, see Figures 8, 11, 18, 21). This behavior warrants careful consideration.

Classical numerical solvers, despite their remarkable accuracy, ultimately rely on spatial and temporal discretization that introduces some degree of numerical error. In contrast, PINNs approximate solutions in a continuous space-time domain without explicit discretization. Our results suggest an interesting possibility: as second-order optimization enables more stable optimization of PINNs toward exact satisfaction of the governing equations, the resulting solutions might be approaching the true analytical solutions more closely than previously thought possible.

This observation is particularly relevant for turbulent flows, where our spectral analysis reveals that PINNs maintain higher spectral energy content at fine scales compared to numerical solutions, even at high grid resolutions (see Figure 3b). While our spectral analysis provides compelling evidence for this phenomenon, several important questions remain open for future investigation. A rigorous theoretical framework will be needed to precisely characterize the relationship between PINNs’ continuous approximations and discretized numerical solutions. Additionally, careful analysis of the asymptotic convergence properties of PINNs solutions as training losses approach zero could provide valuable insights into their fundamental approximation capabilities. Understanding these aspects could open new directions for solving challenging PDEs where discretization effects significantly impact solution accuracy.

**Ablation studies.** We conduct systematic experiments to evaluate SOAP’s performance across different architectures and hyperparameter settings, establishing the robustness of our approach. Our first investigation examines SOAP’s effectiveness across three representative architectures: standard MLP, modified MLP [7], and PirateNet [28]. As shown in the top panel of Figure 4, testing each architecture on four benchmark PDEs (Wave, Burgers, Allen-Cahn, and KdV equations), we find that SOAP consistently improves accuracy compared to Adam optimization regardless of the

underlying network backbones. In particular, PirateNet seems to be the most effective architecture across all test cases, leading to its selection for our main experiments.

As illustrated in the bottom panel of Figure 4, our results of SOAP’s hyperparameters reveal two critical factors affecting performance. The preconditioner update frequency presents a clear trade-off between accuracy and computational cost. While more frequent updates yield better results, the improvements diminish beyond an update frequency of 2, which we selected as the optimal balance for our experiments. The momentum parameter  $\beta_1$  proved especially crucial: high momentum ( $\beta_1 = 0.99$ ) consistently achieves the best results, while low momentum ( $\beta_1=0.01$ ) significantly degrades performance across all test cases.

For completeness, we also compared SOAP against ConFiG [34], a recently proposed method for addressing gradient conflicts in PINNs that has demonstrated relative good performance compared to established baselines such as PCGrad [1] and IMTL-G [35] in multi-task learning. Despite its promising theoretical foundations, ConFiG showed significant sensitivity to hyperparameter settings in our experiments, often resulting in unstable training and inconsistent performance. These results highlight the practical advantages of SOAP’s more robust optimization approach.

**Computational Cost.** While SOAP requires approximately 2x longer training time compared to baselines (Table 5), our focus is exploring the performance frontier of PINNs through extended training to full convergence. Impressively, error and loss convergence curves (Appendix F.6) indicate that SOAP typically achieves rapid initial convergence, reaching a reasonable accuracy (approximately  $10^{-4}$ ) within the first 10,000 iterations, followed by gradual error reduction in subsequent iterations. This suggests the potential for reducing training time by up to 10x while maintaining competitive performance. These findings motivate future research into designing computationally efficient optimization algorithms and training strategies for PINNs, paving the way for practical and scalable applications in complex physics simulations.

## 5 Conclusion and Discussion

This work advances our understanding of gradient conflicts in multi-task learning through the lens of physics-informed neural networks. Our theoretical analysis reveals fundamental challenges that arise when different loss terms push parameters in opposing directions – a situation also common across a broad spectrum of deep learning applications from computer vision to natural language processing. We show that appropriate preconditioning through second-order information naturally aligns these conflicting gradients, providing a general principle for multi-task optimization. Our implementation through SOAP offers both theoretical guarantees and practical efficiency, leading to breakthrough results including the first successful application of PINNs to high Reynolds number turbulent flows with 2-10x accuracy improvements over existing methods.

An intriguing observation emerged from our investigation of complex PDE systems: while training losses continue to decrease, prediction accuracy against high-resolution numerical solutions tends to plateau. Our spectral analysis of turbulent flows provides compelling evidence that PINNs can capture fine-scale dynamics more accurately than traditional numerical solvers, even at very high grid resolutions. This suggests that PINNs, by learning continuous representations unconstrained by discretization, might be approaching more accurate solutions to the underlying physical equations than previously possible. These findings could have broad implications beyond scientific computing to areas like continuous representation learning.

Building on these insights, several promising research directions emerge. A rigorous theoretical framework characterizing how PINNs approximate solutions in the continuous domain could fundamentally change our understanding of neural networks in scientific computing. While SOAP demonstrates the power of gradient alignment in handling coupled physical constraints, opportunities exist for more efficient preconditioned algorithms that maintain their effectiveness with reduced computational cost. More broadly, our work suggests that the principles of gradient alignment and second-order preconditioning could benefit many deep learning applications involving competing objectives, though challenges remain in scaling these approaches to larger systems. Success in these directions could transform both scientific computing and multi-task optimization.

## Acknowledgment

B.L. would like to acknowledge support from National Key R&D Program of China Grant No. 2024YFA1016000. P.P. and S.W. acknowledge support from the US Department of Energy under the Advanced Scientific Computing Research program (grant DE-SC0024563), the Nvidia Academic Grant Program, and the Institute for Foundations of Data Science at Yale University. We also thank the developers of the software that enabled our research, including JAX [36], Matplotlib [37], and NumPy [38].

## References

- [1] Tianhe Yu, Saurabh Kumar, Abhishek Gupta, Sergey Levine, Karol Hausman, and Chelsea Finn. Gradient surgery for multi-task learning. *Advances in Neural Information Processing Systems*, 33:5824–5836, 2020.
- [2] Bo Liu, Xingchao Liu, Xiaojie Jin, Peter Stone, and Qiang Liu. Conflict-averse gradient descent for multi-task learning. *Advances in Neural Information Processing Systems*, 34:18878–18890, 2021.
- [3] Guangyuan Shi, Qimai Li, Wenlong Zhang, Jiabin Chen, and Xiao-Ming Wu. Recon: Reducing conflicting gradients from the root for multi-task learning. *arXiv preprint arXiv:2302.11289*, 2023.
- [4] Nikhil Vyas, Depen Morwani, Rosie Zhao, Itai Shapira, David Brandfonbrener, Lucas Janson, and Sham Kakade. Soap: Improving and stabilizing shampoo using adam. *arXiv preprint arXiv:2409.11321*, 2024.
- [5] Maziar Raissi, Paris Perdikaris, and George E Karniadakis. Physics-informed neural networks: A deep learning framework for solving forward and inverse problems involving nonlinear partial differential equations. *Journal of Computational Physics*, 378:686–707, 2019.
- [6] Andreas Griewank and Andrea Walther. *Evaluating derivatives: principles and techniques of algorithmic differentiation*. SIAM, 2008.
- [7] Sifan Wang, Yujun Teng, and Paris Perdikaris. Understanding and mitigating gradient flow pathologies in physics-informed neural networks. *SIAM Journal on Scientific Computing*, 43(5):A3055–A3081, 2021.
- [8] Sifan Wang, Xinling Yu, and Paris Perdikaris. When and why PINNs fail to train: A neural tangent kernel perspective. *Journal of Computational Physics*, 449:110768, 2022.
- [9] Wensheng Li, Chao Zhang, Chuncheng Wang, Hanting Guan, and Dacheng Tao. Revisiting pinns: Generative adversarial physics-informed neural networks and point-weighting method. *arXiv preprint arXiv:2205.08754*, 2022.
- [10] Wenqian Chen, Amanda A Howard, and Panos Stinis. Self-adaptive weights based on balanced residual decay rate for physics-informed neural networks and deep operator networks. *arXiv preprint arXiv:2407.01613*, 2024.
- [11] Sokratis J Anagnostopoulos, Juan Diego Toscano, Nikolaos Stergiopoulos, and George Em Karniadakis. Residual-based attention in physics-informed neural networks. *Computer Methods in Applied Mechanics and Engineering*, 421:116805, 2024.
- [12] Li Liu, Shengping Liu, Hui Xie, Fansheng Xiong, Tengchao Yu, Mengjuan Xiao, Lufeng Liu, and Heng Yong. Discontinuity computing using physics-informed neural networks. *Journal of Scientific Computing*, 98(1):22, 2024.
- [13] Jiahao Song, Wenbo Cao, Fei Liao, and Weiwei Zhang. Vw-pinns: A volume weighting method for pde residuals in physics-informed neural networks. *Acta Mechanica Sinica*, 41(3):324140, 2025.
- [14] John Duchi, Elad Hazan, and Yoram Singer. Adaptive subgradient methods for online learning and stochastic optimization. *Journal of machine learning research*, 12(7), 2011.
- [15] Elad Hazan, Amit Agarwal, and Satyen Kale. Logarithmic regret algorithms for online convex optimization. *Machine Learning*, 69(2):169–192, 2007.
- [16] James Martens and Roger Grosse. Optimizing neural networks with kronecker-factored approximate curvature. In *International conference on machine learning*, pages 2408–2417. PMLR, 2015.
- [17] Naman Agarwal, Brian Bullins, Xinyi Chen, Elad Hazan, Karan Singh, Cyril Zhang, and Yi Zhang. The case for full-matrix adaptive regularization. *arXiv preprint arXiv:1806.02958*, pages 404–413, 2018.
- [18] Vineet Gupta, Tomer Koren, and Yoram Singer. Shampoo: Preconditioned stochastic tensor optimization. In *International Conference on Machine Learning*, pages 1842–1850. PMLR, 2018.
- [19] Rohan Anil, Vineet Gupta, Tomer Koren, Kevin Regan, and Yoram Singer. Scalable second order optimization for deep learning. *arXiv preprint arXiv:2002.09018*, 2020.
- [20] Depen Morwani, Itai Shapira, Nikhil Vyas, Eran Malach, Sham Kakade, and Lucas Janson. A new perspective on shampoo’s preconditioner. *arXiv preprint arXiv:2406.17748*, 2024.
- [21] Adepu Ravi Sankar, Yash Khasbage, Rahul Vigneswaran, and Vineeth N Balasubramanian. A deeper look at the hessian eigenspectrum of deep neural networks and its applications to regularization. In *Proceedings of the AAAI Conference on Artificial Intelligence*, volume 35, pages 9481–9488, 2021.
- [22] Keller Jordan, Yuchen Jin, Vlado Boza, Jiacheng You, Franz Cesista, Laker Newhouse, and Jeremy Bernstein. Muon: An optimizer for hidden layers in neural networks, 2024.

- [23] U Ghia, K.N Ghia, and C.T Shin. High-re solutions for incompressible flow using the navier-stokes equations and a multigrid method. *Journal of Computational Physics*, 48(3):387–411, 1982.
- [24] Johannes Müller and Marius Zeinhofer. Achieving high accuracy with pinns via energy natural gradient descent. In *International Conference on Machine Learning*, pages 25471–25485. PMLR, 2023.
- [25] Anas Jnini, Flavio Vella, and Marius Zeinhofer. Gauss-newton natural gradient descent for physics-informed computational fluid dynamics. *arXiv preprint arXiv:2402.10680*, 2024.
- [26] Jorge F Urbán, Petros Stefanou, and José A Pons. Unveiling the optimization process of physics informed neural networks: How accurate and competitive can pinns be? *Journal of Computational Physics*, 523:113656, 2025.
- [27] Sifan Wang, Shyam Sankaran, Hanwen Wang, and Paris Perdikaris. An expert’s guide to training physics-informed neural networks. *arXiv preprint arXiv:2308.08468*, 2023.
- [28] Sifan Wang, Bowen Li, Yuhan Chen, and Paris Perdikaris. Piratenets: Physics-informed deep learning with residual adaptive networks. *arXiv preprint arXiv:2402.00326*, 2024.
- [29] Sifan Wang, Hanwen Wang, Jacob H Seidman, and Paris Perdikaris. Random weight factorization improves the training of continuous neural representations. *arXiv preprint arXiv:2210.01274*, 2022.
- [30] Suchuan Dong and Naxian Ni. A method for representing periodic functions and enforcing exactly periodic boundary conditions with deep neural networks. *Journal of Computational Physics*, 435:110242, 2021.
- [31] Diederik P Kingma and Jimmy Ba. Adam: A method for stochastic optimization. *arXiv preprint arXiv:1412.6980*, 2014.
- [32] Sifan Wang, Shyam Sankaran, and Paris Perdikaris. Respecting causality is all you need for training physics-informed neural networks. *arXiv preprint arXiv:2203.07404*, 2022.
- [33] Aditi S Krishnapriyan, Amir Gholami, Shandian Zhe, Robert M Kirby, and Michael W Mahoney. Characterizing possible failure modes in physics-informed neural networks. *arXiv preprint arXiv:2109.01050*, 2021.
- [34] Qiang Liu, Mengyu Chu, and Nils Thuerey. Config: Towards conflict-free training of physics informed neural networks. *arXiv preprint arXiv:2408.11104*, 2024.
- [35] Liyang Liu, Yi Li, Zhanghui Kuang, J Xue, Yimin Chen, Wenming Yang, Qingmin Liao, and Wayne Zhang. Towards impartial multi-task learning. *iclr*, 2021.
- [36] James Bradbury, Roy Frostig, Peter Hawkins, Matthew James Johnson, Chris Leary, Dougal Maclaurin, George Necula, Adam Paszke, Jake VanderPlas, Skye Wanderman-Milne, and Qiao Zhang. JAX: composable transformations of Python+NumPy programs, 2018.
- [37] John D Hunter. Matplotlib: A 2D graphics environment. *IEEE Annals of the History of Computing*, 9(03):90–95, 2007.
- [38] Charles R Harris, K Jarrod Millman, Stéfan J van der Walt, Ralf Gommers, Pauli Virtanen, David Cournapeau, Eric Wieser, Julian Taylor, Sebastian Berg, Nathaniel J Smith, et al. Array programming with numpy. *Nature*, 585(7825):357–362, 2020.
- [39] Maziar Raissi, Alireza Yazdani, and George Em Karniadakis. Hidden fluid mechanics: Learning velocity and pressure fields from flow visualizations. *Science*, 367(6481):1026–1030, 2020.
- [40] Muhammad M Almajid and Moataz O Abu-Al-Saud. Prediction of porous media fluid flow using physics informed neural networks. *Journal of Petroleum Science and Engineering*, 208:109205, 2022.
- [41] Hamidreza Eivazi, Mojtaba Tahani, Philipp Schlatter, and Ricardo Vinuesa. Physics-informed neural networks for solving reynolds-averaged navier–stokes equations. *Physics of Fluids*, 34(7), 2022.
- [42] Zhen Cao, Kai Liu, Kun Luo, Sifan Wang, Liang Jiang, and Jianren Fan. Surrogate modeling of multi-dimensional premixed and non-premixed combustion using pseudo-time stepping physics-informed neural networks. *Physics of Fluids*, 36(11), 2024.
- [43] Jiakuan Xu, Han Wei, and Hua Bao. Physics-informed neural networks for studying heat transfer in porous media. *International Journal of Heat and Mass Transfer*, 217:124671, 2023.
- [44] Hassan Bararnia and Mehdi Esmaeilpour. On the application of physics informed neural networks (pinn) to solve boundary layer thermal-fluid problems. *International Communications in Heat and Mass Transfer*, 132:105890, 2022.
- [45] Gargya Gokhale, Bert Claessens, and Chris Develder. Physics informed neural networks for control oriented thermal modeling of buildings. *Applied Energy*, 314:118852, 2022.

- [46] Georgios Kissas, Yibo Yang, Eileen Hwuang, Walter R Witschey, John A Detre, and Paris Perdikaris. Machine learning in cardiovascular flows modeling: Predicting arterial blood pressure from non-invasive 4D flow MRI data using physics-informed neural networks. *Computer Methods in Applied Mechanics and Engineering*, 358:112623, 2020.
- [47] Xuelan Zhang, Baoyan Mao, Yue Che, Jiaheng Kang, Mingyao Luo, Aike Qiao, Youjun Liu, Hitomi Anzai, Makoto Ohta, Yuting Guo, et al. Physics-informed neural networks (pinns) for 4d hemodynamics prediction: an investigation of optimal framework based on vascular morphology. *Computers in Biology and Medicine*, 164:107287, 2023.
- [48] Federica Caforio, Francesco Regazzoni, Stefano Pagani, Elias Karabelas, Christoph Augustin, Gundolf Haase, Gernot Plank, and Alfio Quarteroni. Physics-informed neural network estimation of material properties in soft tissue nonlinear biomechanical models. *Computational Mechanics*, pages 1–27, 2024.
- [49] Enrui Zhang, Ming Dao, George Em Karniadakis, and Subra Suresh. Analyses of internal structures and defects in materials using physics-informed neural networks. *Science advances*, 8(7):eabk0644, 2022.
- [50] Hyogu Jeong, Jinshuai Bai, Chanaka Prabuddha Batuwatta-Gamage, Charith Rathnayaka, Ying Zhou, and YuanTong Gu. A physics-informed neural network-based topology optimization (pinnto) framework for structural optimization. *Engineering Structures*, 278:115484, 2023.
- [51] Haoteng Hu, Lehua Qi, and Xujiang Chao. Physics-informed neural networks (pinn) for computational solid mechanics: Numerical frameworks and applications. *Thin-Walled Structures*, page 112495, 2024.
- [52] Alexander Kovacs, Lukas Exl, Alexander Kornell, Johann Fischbacher, Markus Hovorka, Markus Gusenbauer, Leoni Breth, Harald Oezelt, Masao Yano, Noritsugu Sakuma, et al. Conditional physics informed neural networks. *Communications in Nonlinear Science and Numerical Simulation*, 104:106041, 2022.
- [53] Arbaaz Khan and David A Lowther. Physics informed neural networks for electromagnetic analysis. *IEEE Transactions on Magnetics*, 58(9):1–4, 2022.
- [54] Marco Baldan, Paolo Di Barba, and David A Lowther. Physics-informed neural networks for inverse electromagnetic problems. *IEEE Transactions on Magnetics*, 59(5):1–5, 2023.
- [55] Jonthan D Smith, Zachary E Ross, Kamyar Azizzadenesheli, and Jack B Muir. Hyposvi: Hypocentre inversion with stein variational inference and physics informed neural networks. *Geophysical Journal International*, 228(1):698–710, 2022.
- [56] Chao Song and Yanghua Wang. Simulating seismic multifrequency wavefields with the fourier feature physics-informed neural network. *Geophysical Journal International*, 232(3):1503–1514, 2023.
- [57] Pu Ren, Chengping Rao, Su Chen, Jian-Xun Wang, Hao Sun, and Yang Liu. Seismicnet: Physics-informed neural networks for seismic wave modeling in semi-infinite domain. *Computer Physics Communications*, 295:109010, 2024.
- [58] Vincent Sitzmann, Julien Martel, Alexander Bergman, David Lindell, and Gordon Wetzstein. Implicit neural representations with periodic activation functions. *Advances in Neural Information Processing Systems*, 33:7462–7473, 2020.
- [59] Rizal Fathony, Anit Kumar Sahu, Devin Willmott, and J Zico Kolter. Multiplicative filter networks. In *International Conference on Learning Representations*, 2021.
- [60] Ben Moseley, Andrew Markham, and Tarje Nissen-Meyer. Finite basis physics-informed neural networks (fbpinns): a scalable domain decomposition approach for solving differential equations. *arXiv preprint arXiv:2107.07871*, 2021.
- [61] Namgyu Kang, Byeonghyeon Lee, Youngjoon Hong, Seok-Bae Yun, and Eunbyung Park. Pixel: Physics-informed cell representations for fast and accurate pde solvers. *arXiv preprint arXiv:2207.12800*, 2022.
- [62] Junwoo Cho, Seungtae Nam, Hyunmo Yang, Seok-Bae Yun, Youngjoon Hong, and Eunbyung Park. Separable physics-informed neural networks. *Advances in Neural Information Processing Systems*, 36, 2024.
- [63] Mohammad Amin Nabian, Rini Jasmine Gladstone, and Hadi Meidani. Efficient training of physics-informed neural networks via importance sampling. *Computer-Aided Civil and Infrastructure Engineering*, 2021.
- [64] Arka Daw, Jie Bu, Sifan Wang, Paris Perdikaris, and Anuj Karpatne. Rethinking the importance of sampling in physics-informed neural networks. *arXiv preprint arXiv:2207.02338*, 2022.
- [65] Chenxi Wu, Min Zhu, Qinyang Tan, Yadhu Kartha, and Lu Lu. A comprehensive study of non-adaptive and residual-based adaptive sampling for physics-informed neural networks. *Computer Methods in Applied Mechanics and Engineering*, 403:115671, 2023.

- [66] Yongcun Song, Xiaoming Yuan, and Hangrui Yue. The admm-pinns algorithmic framework for nonsmooth pde-constrained optimization: a deep learning approach. *SIAM Journal on Scientific Computing*, 46(6):C659–C687, 2024.
- [67] Colby L Wight and Jia Zhao. Solving Allen-Cahn and Cahn-Hilliard equations using the adaptive physics informed neural networks. *arXiv preprint arXiv:2007.04542*, 2020.
- [68] Wenbo Cao and Weiwei Zhang. Tsonn: Time-stepping-oriented neural network for solving partial differential equations. *arXiv preprint arXiv:2310.16491*, 2023.
- [69] Pao-Hsiung Chiu, Jian Cheng Wong, Chinchun Ooi, My Ha Dao, and Yew-Soon Ong. Can-pinn: A fast physics-informed neural network based on coupled-automatic-numerical differentiation method. *Computer Methods in Applied Mechanics and Engineering*, 395:114909, 2022.
- [70] Xinquan Huang and Tariq Alkhalifah. Efficient physics-informed neural networks using hash encoding. *Journal of Computational Physics*, page 112760, 2024.
- [71] Ehsan Kharazmi, Zhongqiang Zhang, and George Em Karniadakis. hp-vpinns: Variational physics-informed neural networks with domain decomposition. *Computer Methods in Applied Mechanics and Engineering*, 374:113547, 2021.
- [72] Ravi G Patel, Indu Manickam, Nathaniel A Trask, Mitchell A Wood, Myoungkyu Lee, Ignacio Tomas, and Eric C Cyr. Thermodynamically consistent physics-informed neural networks for hyperbolic systems. *Journal of Computational Physics*, 449:110754, 2022.
- [73] Jeremy Yu, Lu Lu, Xuhui Meng, and George Em Karniadakis. Gradient-enhanced physics-informed neural networks for forward and inverse pde problems. *Computer Methods in Applied Mechanics and Engineering*, 393:114823, 2022.
- [74] Hwijae Son, Jin Woo Jang, Woo Jin Han, and Hyung Ju Hwang. Sobolev training for physics informed neural networks. *arXiv preprint arXiv:2101.08932*, 2021.
- [75] Igor Molybog, Peter Albert, Moya Chen, Zachary DeVito, David Esiobu, Naman Goyal, Punit Singh Koura, Sharan Narang, Andrew Poulton, Ruan Silva, et al. A theory on adam instability in large-scale machine learning. *arXiv preprint arXiv:2304.09871*, 2023.
- [76] Hanxu Zhou, Zhou Qixuan, Tao Luo, Yaoyu Zhang, and Zhi-Qin Xu. Towards understanding the condensation of neural networks at initial training. *Advances in Neural Information Processing Systems*, 35:2184–2196, 2022.
- [77] Zheng-an Chen and Tao Luo. On the dynamics of three-layer neural networks: initial condensation. *arXiv preprint arXiv:2402.15958*, 2024.
- [78] Anas Barakat and Pascal Bianchi. Convergence and dynamical behavior of the adam algorithm for nonconvex stochastic optimization. *SIAM Journal on Optimization*, 31(1):244–274, 2021.
- [79] Lukas Balles and Philipp Hennig. Dissecting adam: The sign, magnitude and variance of stochastic gradients. In *International Conference on Machine Learning*, pages 404–413. PMLR, 2018.
- [80] Sokratis J Anagnostopoulos, Juan Diego Toscano, Nikolaos Stergiopoulos, and George Em Karniadakis. Residual-based attention and connection to information bottleneck theory in pinns. *arXiv preprint arXiv:2307.00379*, 2023.
- [81] Xenofon Karakonstantis, Diego Caviedes-Nozal, Antoine Richard, and Efrén Fernández-Grande. Room impulse response reconstruction with physics-informed deep learning. *The Journal of the Acoustical Society of America*, 155(2):1048–1059, 2024.
- [82] Jiaming Zhang, David Dalton, Hao Gao, and Dirk Husmeier. Physics-informed deep learning based on the finite difference method for efficient and accurate numerical solution of partial differential equations.
- [83] Matthew Tancik, Pratul P Srinivasan, Ben Mildenhall, Sara Fridovich-Keil, Nithin Raghavan, Utkarsh Singhal, Ravi Ramamoorthi, Jonathan T Barron, and Ren Ng. Fourier features let networks learn high frequency functions in low dimensional domains. *arXiv preprint arXiv:2006.10739*, 2020.
- [84] Sifan Wang, Hanwen Wang, and Paris Perdikaris. On the eigenvector bias of fourier feature networks: From regression to solving multi-scale PDEs with physics-informed neural networks. *Computer Methods in Applied Mechanics and Engineering*, 384:113938, 2021.
- [85] Xavier Glorot and Yoshua Bengio. Understanding the difficulty of training deep feedforward neural networks. In *Proceedings of the thirteenth international conference on artificial intelligence and statistics*, pages 249–256, 2010.
- [86] Tim Salimans and Durk P Kingma. Weight normalization: A simple reparameterization to accelerate training of deep neural networks. *Advances in neural information processing systems*, 29, 2016.

- [87] Tobin A Driscoll, Nicholas Hale, and Lloyd N Trefethen. Chebfun guide, 2014.
- [88] Syver Døving Agdestein, Simone Ciarella, and Benjamin Sanderse. IncompressibleNavierStokes.jl, November 2024.
- [89] Levi McClenny and Ulisses Braga-Neto. Self-adaptive physics-informed neural networks using a soft attention mechanism. *arXiv preprint arXiv:2009.04544*, 2020.
- [90] Revanth Matthey and Susanta Ghosh. A novel sequential method to train physics informed neural networks for allen cahn and cahn hilliard equations. *Computer Methods in Applied Mechanics and Engineering*, 390:114474, 2022.
- [91] Vasilii A Es' kin, Danil V Davydov, Ekaterina D Egorova, Alexey O Malkhanov, Mikhail A Akhukov, and Mikhail E Smorkalov. About optimal loss function for training physics-informed neural networks under respecting causality. *arXiv preprint arXiv:2304.02282*, 2023.
- [92] Norman J Zabusky and Martin D Kruskal. Interaction of " solitons" in a collisionless plasma and the recurrence of initial states. *Physical review letters*, 15(6):240, 1965.

## A Nomenclature

Table 2: Notation used throughout the paper. We use uppercase letters for matrices and lowercase letters for their vectorized forms. All gradients and Hessians are with respect to the loss function  $\mathcal{L}$ .

Symbol	Description
$\mathcal{L}$	Loss function
$\theta$	Neural network parameters
$W$	Weight matrix for a given layer
$w$	Vectorized weight matrix, $w = \text{Vec}(W)$
$G$	Gradient matrix, $G = \nabla_W \mathcal{L}$
$g$	Vectorized gradient, $g = \text{Vec}(G)$
$H$	Hessian matrix, $H = \nabla_{\theta}^2 \mathcal{L}$
$H_{\text{Ada}}$	Full Adagrad preconditioner matrix
$H_{\text{GN}}$	Gauss-Newton approximation of the Hessian
$\mathcal{A}$	Gradient alignment score between loss components

## B Related Work

Physics-informed neural networks (PINNs) have emerged as a powerful paradigm in scientific machine learning by incorporating physical principles through carefully designed loss functions. These loss functions act as soft constraints, guiding neural networks to learn solutions that respect underlying physical laws while simultaneously fitting experimental data. The elegance and versatility of PINNs have led to their widespread adoption in solving both forward and inverse problems involving partial differential equations (PDEs). Their success spans numerous domains in computational science, from fluid mechanics [39–42], heat transfer [43–45] to bio-engineering [46–48] and materials science [49–51]. The impact of PINNs extends even further, with applications in electromagnetics [52–54], geosciences [55–57], etc.

Despite their broad applications, PINNs currently face limitations in convergence speed and accuracy that affect their reliability as forward PDE solvers. This has motivated extensive research efforts to enhance their performance through various methodological innovations. One prominent line of research focuses on developing self-adaptive loss weighting schemes to address unbalanced back-propagated gradients during training [7, 8]. While various strategies have been proposed [7–13, 27], they primarily address gradient magnitude imbalances rather than directional conflicts, with a recent exception being [34] whose effectiveness is hereby shown to be limited. Other advances include architectural innovations [7, 28, 58–62], improved training processes [24–26, 33, 63–68], and alternative learning objectives [69–74]. However, the fundamental challenge of resolving directional gradient conflicts remains largely unaddressed.

## C Connection between SOAP and Newton’s method

For our purpose, we begin by noting that there exists a one-to-one correspondence between the original parameter space and the rotated space that preserves the matrix-vector multiplication.

**Lemma 2.** *Let  $Q_L \in \mathbb{R}^{m \times m}$  and  $Q_R \in \mathbb{R}^{n \times n}$  be two orthogonal matrices. For any matrix  $A \in \mathbb{R}^{mn \times mn}$  and vector  $v \in \mathbb{R}^{mn}$ , define  $\tilde{v} := (Q_L \otimes Q_R)v$  and  $\tilde{A} := (Q_L \otimes Q_R)A(Q_L^T \otimes Q_R^T)$ . Then there holds*

$$\tilde{A}v = (Q_L \otimes Q_R)Av = \tilde{A}\tilde{v}.$$

The proof follows directly by applying the transformation  $Q_L \otimes Q_R$  to  $Av$  and the definitions of  $\tilde{A}$  and  $\tilde{v}$ . Building on the above lemma, one can easily transform the preconditioned gradient descent in the original space to the rotated one and vice versa.

**Corollary 1.** *Let  $W_t, G_t \in \mathbb{R}^{m \times n}$  be the weight matrix and gradient matrix for a layer at iteration  $t$ , respectively, with vectorizations  $w_t = \text{vec}(W_t)$  and  $g_t = \text{vec}(G_t)$ . The preconditioned gradient descent update:*

$$w_{t+1} = w_t - \eta H^{-1}g_t, \tag{C.1}$$

is equivalent to performing preconditioning in the rotated space:

$$\tilde{w}_{t+1} = \tilde{w}_t - \eta \tilde{H}^{-1}\tilde{g}_t, \tag{C.2}$$

where  $H \in \mathbb{R}^{mn \times mn}$  is the preconditioner, and  $\tilde{w}$ ,  $\tilde{g}$ , and  $\tilde{H}$  are the rotated weight, gradient, and preconditioner defined by the transformations in Lemma 2.

**Proposition 3.** *Let  $L_t = \mathbb{E}[G_t G_t^T]$  and  $R_t = \mathbb{E}[G_t^T G_t]$  have eigendecompositions  $L_t = Q_L \Lambda_L Q_L^T$  and  $R_t = Q_R \Lambda_R Q_R^T$ . Under the assumption of Lemma 5, the equivalent preconditioner in the rotated space is diagonal, i.e.,  $\tilde{H}_{GN} = \text{diag}(\tilde{H}_{GN})$ .*

*Proof.* The proof follows from the combination of Lemma 2 and Lemma 5. First, we express  $H_{GN}$  using the Kronecker approximation:

$$H_{GN} = L_t^{1/2} \otimes R_t^{1/2} / \text{Tr}(\mathbb{E}[GG^T]). \tag{C.3}$$

Then, we derive the rotated preconditioner:

$$\begin{aligned} \tilde{H}_{GN} &= (Q_L \otimes Q_R) H_{GN} (Q_L^T \otimes Q_R^T) \\ &= (Q_L \otimes Q_R) (L_t^{1/2} \otimes R_t^{1/2}) (Q_L^T \otimes Q_R^T) / \text{Tr}(\mathbb{E}[GG^T]) \\ &= (Q_L L_t^{1/2} Q_L^T) \otimes (Q_R R_t^{1/2} Q_R^T) / \text{Tr}(\mathbb{E}[\Lambda_L]) \\ &= \Lambda_L^{1/2} \otimes \Lambda_R^{1/2} / \text{Tr}(\mathbb{E}[\Lambda_L]). \end{aligned}$$

The final expression shows that  $\tilde{H}_{Ada}$  is diagonal, as it is the Kronecker product of diagonal matrices scaled by a scalar factor.  $\square$

Finally, we connect our analysis to Adam’s update rule by adapting the following result from Molybog et al [75]:

**Proposition 4** (Adapt from [75]). *Suppose that  $\theta^*$  is a local minimum and assume that  $\theta - \theta^* \sim \mathcal{N}(0, \sigma^2 I)$ . For Adam update rule denoted by  $\theta_{t+1} = \theta_t - \eta \text{Adam}(g_t)$ , we have*

$$\text{Adam}(g_t) \approx \text{diag}(H)^{-1} g_t. \tag{C.4}$$

*Proof.* The Adam optimizer follows the update rule:

$$\begin{aligned} m_t &= \beta_1 m_{t-1} + (1 - \beta_1)g_t, \\ v_t &= \beta_2 v_{t-1} + (1 - \beta_2)g_t \odot g_t, \\ \hat{m}_t &= m_t / (1 - \beta_1^t), \\ \hat{v}_t &= v_t / (1 - \beta_2^t), \\ \theta_t &= \theta_t - 1 - \eta \hat{m}_t / (\sqrt{\hat{v}_t} + \epsilon). \end{aligned}$$

Taking a first-order Taylor expansion of the gradient around a local minimum  $\theta^*$ :

$$g_\theta \approx g_{\theta^*} + H_{\theta^*} (\theta - \theta^*) \approx H_{\theta^*} (\theta - \theta^*).$$

This yields

$$g_\theta g_\theta^\top \approx H_{\theta^*} (\theta - \theta^*) (\theta - \theta^*)^\top H_{\theta^*}^\top.$$

Under our assumption that  $\theta - \theta^* \sim \mathcal{N}(0, \sigma^2 I)$ ,

$$\mathbb{E} [g_\theta g_\theta^\top] \approx H_{\theta^*} \mathbb{E} [(\theta - \theta^*) (\theta - \theta^*)^\top] H_{\theta^*}^\top = \sigma^2 H_{\theta^*} H_{\theta^*}^\top.$$

By construction,  $v_t$  approximates the diagonal of  $\mathbb{E}_{\theta \sim \theta_\tau} [g_\theta g_\theta^\top]$ , where  $\theta_\tau$  represents the distribution of model weights over the past  $O(1/(1 - \beta_2))$  steps:

$$v_t \approx \text{diag} (\mathbb{E}_{\theta \sim \theta_\tau} [g_\theta g_\theta^\top]) \approx \sigma^2 \text{diag}(H_{\theta^*}^2).$$

Finally, assuming  $m_t \approx g_t$ :

$$\text{Adam}(g_t) \approx \frac{m_t}{\sqrt{v_t} + \varepsilon} \approx \frac{m_t}{\sqrt{v_t}} \approx \text{diag}(H)^{-1} g_t.$$

□

**Theorem 2.** *Under Assumption 1 and the conditions of Proposition 4,*

$$w_{t+1} = w_t - \eta \text{Soap}(g_t) \approx w_t - \eta H^{-1} g_t. \quad (\text{C.5})$$

*Proof.* Combining Propositions 3 and 4, we obtain

$$\text{Adam}(\tilde{G}_t) \approx \text{diag}(\tilde{H})^{-1} \tilde{g}_t \approx \text{diag}(\tilde{H}_{\text{GN}})^{-1} \tilde{g}_t = \tilde{H}_{\text{GN}}^{-1} \tilde{g}_t \approx \tilde{H}^{-1} \tilde{g}_t. \quad (\text{C.6})$$

By Corollary 1, this is equivalent to the Newton update in the original space:

$$w_{t+1} = w_t - H^{-1} g_t. \quad (\text{C.7})$$

As a direction implication, the Hessian matrix is approximately diagonal in the rotated space. □

## D Analysis of Intra-step Gradient Alignment

We present some preliminary analysis to understand intra-step gradient conflicts in training PINNs via standard gradient descent, Adam [31], and Shampoo algorithms [18], and how SOAP can effectively resolve them during training. For simplicity, we consider the simplest case of using PINNs with the two-layer NN to solve the one-dimensional Laplace equation and focus on the analysis of the intra-step gradient alignment (3.3) with small initialization. The analysis can be easily extended to other types of PDEs. Following the general setup in Section 2, without loss of generality, we consider 1D Laplace equation as follows

$$\begin{cases} \Delta u = u'' = 0 & \text{on } [-1, 1], \\ u(\pm 1) = g_{\pm 1}. \end{cases} \quad (\text{D.1})$$

We approximate the solution  $u(x)$  by a two-layer network with width  $N$ :

$$u(x, \theta) = \sum_{i=1}^N a_i \sigma(w_i x) = \mathbf{a} \cdot \sigma(\mathbf{w}x), \quad (\text{D.2})$$

where  $\mathbf{a} = (a_1, \dots, a_N)$ ,  $\mathbf{w} = (w_1, \dots, w_N) \in \mathbb{R}^N$ , and  $\theta = (\mathbf{a}, \mathbf{w}) \in \mathbb{R}^{2N}$ . Moreover, we limit ourselves to the activation function  $\sigma(x) = \tanh(x)$ . In this case, the loss (2.5) reduces to

$$\min_{\theta=(\mathbf{a}, \mathbf{w})} \mathcal{L}(\theta) = \underbrace{\frac{1}{N_r} \sum_{p=1}^{N_r} |u''(x_p, \theta)|^2}_{\mathcal{L}_r(\theta)} + \frac{1}{2} \underbrace{\sum_{s=\pm 1} |u(s, \theta) - g_s|^2}_{\mathcal{L}_{bc}(\theta)}. \quad (\text{D.3})$$

To analyze the gradient conflict phenomenon in training PINNs, we consider the *small initialization* regime.

**Assumption 2.** The weights  $a_i, w_i$  are initialized by i.i.d. Gaussian  $\mathcal{N}(0, \varepsilon^2)$  with small  $\varepsilon = o(1)$ .

This allows us to introduce the normalized parameters:

$$\bar{\mathbf{a}} = \varepsilon^{-1} \mathbf{a}, \quad \bar{\mathbf{w}} = \varepsilon^{-1} \mathbf{w},$$

initialized as standard Gaussian.

**Lemma 3.** Under small initialization, the gradients of the residual and boundary loss terms can be approximated as:

$$\nabla_{\theta} \mathcal{L}_r(\theta) = \varepsilon^7 G^r(\bar{\mathbf{a}}, \bar{\mathbf{w}}) + O(\varepsilon^9), \quad (\text{D.4})$$

$$\nabla_{\theta} \mathcal{L}_{bc}(\theta) = \varepsilon G^{bc}(\bar{\mathbf{a}}, \bar{\mathbf{w}}) + O(\varepsilon^3), \quad (\text{D.5})$$

where

$$G^r(\bar{\mathbf{a}}, \bar{\mathbf{w}}) = c_r \bar{\mathbf{a}} \cdot \bar{\mathbf{w}}^{\odot 3} (\bar{\mathbf{w}}^{\odot 3}, 3\bar{\mathbf{a}} \odot \bar{\mathbf{w}}^{\odot 2}), \quad (\text{D.6})$$

$$G^{bc}(\bar{\mathbf{a}}, \bar{\mathbf{w}}) = (g_{-1} - g_1) (\bar{\mathbf{w}}, \bar{\mathbf{a}}). \quad (\text{D.7})$$

Here  $\bar{\mathbf{a}} = \varepsilon^{-1} \mathbf{a}$ ,  $\bar{\mathbf{w}} = \varepsilon^{-1} \mathbf{w}$  are the normalized parameters, and  $G^r, G^{bc}$  are the effective gradient terms.

We remark that these elementary computations also provide insights into the gradient magnitude imbalance discussed in Section 3, noting  $\|\nabla_{\theta} \mathcal{L}_r(\theta)\| = O(\varepsilon^7)$  while  $\|\nabla_{\theta} \mathcal{L}_{bc}(\theta)\| = O(\varepsilon)$ .

*Proof.* We recall the Taylor expansions of the activation function  $\sigma(x) = \tanh(x)$  and its derivatives for later use:

$$\begin{aligned} \sigma(x) &= x - \frac{x^3}{3} + O(x^5), \quad \sigma'(x) = 1 - x^2 + O(x^4), \\ \sigma''(x) &= -2x + \frac{8x^3}{3} + O(x^5), \quad \sigma'''(x) = -2 + 8x^2 + O(x^4). \end{aligned} \quad (\text{D.8})$$

The gradient of loss function  $\mathcal{L}(\theta)$  consists of two parts computed as follows:

$$\nabla_{\theta=(\mathbf{a}, \mathbf{w})} \mathcal{L}_r(\theta) = \frac{2}{N_r} \sum_{p=1}^{N_r} u_{xx}(x_p, \theta) \nabla_{\theta=(\mathbf{a}, \mathbf{w})} u_{xx}(x_p, \theta),$$

and

$$\nabla_{\theta=(\mathbf{a}, \mathbf{w})} \mathcal{L}_{bc}(\theta) = \sum_{s=\pm 1} (u(s, \theta) - g(s)) \nabla_{\theta=(\mathbf{a}, \mathbf{w})} u(s, \theta),$$

with, thanks to (D.2) and (D.8),

$$\nabla_{\mathbf{a}} u(x, \theta) = \sigma(\mathbf{w}\mathbf{x}) = \varepsilon \bar{\mathbf{w}}x + O(\varepsilon^3),$$

$$\nabla_{w_i} u(x, \theta) = a_i \sigma'(w_i x) x = \varepsilon \bar{a}_i x - \varepsilon^3 \bar{a}_i \bar{w}_i^2 x^3 + O(\varepsilon^4),$$

and

$$\nabla_{a_i} u_{xx}(x, \theta) = \sigma''(w_i x) |w_i|^2 = -2\varepsilon^3 \bar{w}_i^3 x + O(\varepsilon^5),$$

$$\begin{aligned} \nabla_{w_i} u_{xx}(\mathbf{x}, \theta) &= a_i \sigma'''(w_i x) |w_i|^2 x + 2a_i \sigma''(w_i x) w_i \\ &= -6\varepsilon^3 \bar{a}_i \bar{w}_i^2 x + O(\varepsilon^5). \end{aligned}$$

We also compute

$$u(x, \theta) = \varepsilon^2 \bar{\mathbf{a}} \cdot \bar{\mathbf{w}}x + O(\varepsilon^4),$$

and

$$u_{xx}(x, \theta) = \sum_i a_i \sigma''(w_i x) |w_i|^2 = -2\varepsilon^4 \sum_i \bar{a}_i \bar{w}_i^3 x + O(\varepsilon^6).$$

For convenience, we define the componentwise power  $\mathbf{x}^{\odot k} = (x_1^k, \dots, x_N^k)$  and product  $\mathbf{x} \odot \mathbf{y} = (x_1 y_1, \dots, x_N y_N)$  for  $\mathbf{x}, \mathbf{y} \in \mathbb{R}^N$ . By the above computation, it follows that at the initialization, there hold

$$\begin{aligned} \nabla_{\theta=(\mathbf{a}, \mathbf{w})} \mathcal{L}_r(\theta) &= \frac{2}{N_r} \sum_{p=1}^{N_r} (-2\varepsilon^4 \bar{\mathbf{a}} \cdot \bar{\mathbf{w}}^{\odot 3} x_p) (-2\varepsilon^3 \bar{\mathbf{w}}^{\odot 3} x_p, -6\varepsilon^3 \bar{\mathbf{a}} \odot \bar{\mathbf{w}}^{\odot 2} x_p) + O(\varepsilon^9) \\ &= \varepsilon^7 \frac{8}{N_r} \sum_{p=1}^{N_r} \bar{\mathbf{a}} \cdot \bar{\mathbf{w}}^{\odot 3} (\bar{\mathbf{w}}^{\odot 3}, 3\bar{\mathbf{a}} \odot \bar{\mathbf{w}}^{\odot 2}) x_p^2 + O(\varepsilon^9), \end{aligned}$$

and

$$\begin{aligned}\nabla_{\theta=(\mathbf{a}, \mathbf{w})} \mathcal{L}_{bc}(\theta) &= \sum_{s=\pm 1} (\varepsilon^2 \bar{\mathbf{a}} \cdot \bar{\mathbf{w}} s + O(\varepsilon^4) - g(s)) (\varepsilon \bar{\mathbf{w}} s + O(\varepsilon^3), \varepsilon \bar{\mathbf{a}} s - \varepsilon^3 \bar{\mathbf{a}} \odot \bar{\mathbf{w}}^{\odot 2} s^3 + O(\varepsilon^4)) \\ &= -\varepsilon \sum_{s=\pm 1} s g(s) (\bar{\mathbf{w}}, \bar{\mathbf{a}}) + O(\varepsilon^3) = \varepsilon (g_{-1} - g_1) (\bar{\mathbf{w}}, \bar{\mathbf{a}}) + O(\varepsilon^3).\end{aligned}$$

We then define constant  $c_r = 8N_r^{-1} \sum_{p=1}^{N_r} x_p^2 > 0$  and the effective gradients

$$G^r(\bar{\mathbf{a}}, \bar{\mathbf{w}}) = (G_a^r(\bar{\mathbf{a}}, \bar{\mathbf{w}}), G_w^r(\bar{\mathbf{a}}, \bar{\mathbf{w}})) = c_r \bar{\mathbf{a}} \cdot \bar{\mathbf{w}}^{\odot 3} (\bar{\mathbf{w}}^{\odot 3}, 3\bar{\mathbf{a}} \odot \bar{\mathbf{w}}^{\odot 2}), \quad (\text{D.9})$$

and

$$G^{bc}(\bar{\mathbf{a}}, \bar{\mathbf{w}}) = (G_a^{bc}(\bar{\mathbf{a}}, \bar{\mathbf{w}}), G_w^{bc}(\bar{\mathbf{a}}, \bar{\mathbf{w}})) = (g_{-1} - g_1) (\bar{\mathbf{w}}, \bar{\mathbf{a}}), \quad (\text{D.10})$$

enabling us to write

$$\nabla_{\theta} \mathcal{L}_r(\theta) = \varepsilon^7 G^r(\bar{\mathbf{a}}, \bar{\mathbf{w}}) + O(\varepsilon^9), \quad \nabla_{\theta} \mathcal{L}_{bc}(\theta) = \varepsilon G^{bc}(\bar{\mathbf{a}}, \bar{\mathbf{w}}) + O(\varepsilon^3). \quad (\text{D.11})$$

□

We are now ready to understand the gradient conflict for various optimizers applied to the residual and boundary loss terms separately.

**Proposition 5.** *At initialization, the alignment score converges to a binary random variable in the infinite width limit:*

$$\lim_{N \rightarrow \infty} \mathcal{A}(\square(\nabla \mathcal{L}_b), \square(\nabla \mathcal{L}_r)) = O(\varepsilon^2) + C_{\square} \begin{cases} \text{sgn}(g_{-1} - g_1) & \text{with prob. } \frac{1}{2}, \\ -\text{sgn}(g_{-1} - g_1) & \text{with prob. } \frac{1}{2}. \end{cases} \quad (\text{D.12})$$

where  $\square = \text{GD, Adam, Shampoo, or Soap}$  denotes the optimizer update rule, and  $C_{\square}$  is a constant depending on the optimizer.

We can see that these optimizers fail to resolve intra-step gradient conflicts in the initialization, aligning with the near-zero initial intra-step gradient scores shown in Figure 2.

*Proof. Gradient descent.* We start with the standard continuous-time gradient descent:

$$\frac{d\theta}{dt} = -\nabla_{\theta} \mathcal{L}(\theta). \quad (\text{D.13})$$

Motivated by [76, 77], under small initialization Assumption 2, in the *initial stage* of training dynamics where the leading-order expansion (D.11) holds for the weights  $\mathbf{a}, \mathbf{w}$ , the gradients  $\nabla_{\theta} \mathcal{L}_r(\theta)$  and  $\nabla_{\theta} \mathcal{L}_{bc}(\theta)$  can be effectively described by  $G^r(\bar{\mathbf{a}}, \bar{\mathbf{w}})$  and  $G^{bc}(\bar{\mathbf{a}}, \bar{\mathbf{w}})$ , respectively, up to some scaling factors, then the gradient flow (D.13) can be approximated by the effective dynamics for the normalized parameter  $\bar{\theta} = (\bar{\mathbf{a}}, \bar{\mathbf{w}})$ :

$$\varepsilon \frac{d\bar{\theta}}{dt} = -(\varepsilon^7 G^r(\bar{\theta}) + \varepsilon G^{bc}(\bar{\theta})). \quad (\text{D.14})$$

Recalling Definition 1, under our assumptions, we have the intra alignment score:

$$\mathcal{A}(\nabla_{\theta} \mathcal{L}_r(\theta), \nabla_{\theta} \mathcal{L}_{bc}(\theta)) = \mathcal{A}(G^r(\bar{\theta}), G^{bc}(\bar{\theta})) + O(\varepsilon^2),$$

where

$$\mathcal{A}(G^r(\bar{\theta}), G^{bc}(\bar{\theta})) = \text{sgn}(\bar{\mathbf{a}} \cdot \bar{\mathbf{w}}^{\odot 3}) \text{sgn}(g_{-1} - g_1) \frac{\sum_i \bar{w}_i^4 + 3 \sum_i \bar{a}_i^2 \bar{w}_i^2}{\sqrt{\sum_i \bar{w}_i^6 + 9 \bar{a}_i^2 \bar{w}_i^4} \sqrt{\sum_i \bar{w}_i^2 + \bar{a}_i^2}}.$$

Then we find that at the initialization, by  $\bar{a}_i, \bar{w}_i \sim \mathcal{N}(0, 1)$  from Assumption 2 and the law of large numbers,

$$\frac{\frac{1}{N} \sum_i \bar{w}_i^4 + 3 \frac{1}{N} \sum_i \bar{a}_i^2 \bar{w}_i^2}{\sqrt{\frac{1}{N} \sum_i \bar{w}_i^6 + 9 \bar{a}_i^2 \bar{w}_i^4} \sqrt{\frac{1}{N} \sum_i \bar{w}_i^2 + \bar{a}_i^2}} \rightarrow \frac{6}{\sqrt{15 + 27\sqrt{2}}} = \frac{3}{\sqrt{21}}, \quad \text{almost surely.}$$

Also, by the symmetry of Gaussian, there holds  $\mathbb{P}(\sum_i \bar{a}_i \bar{w}_i^3 > 0) = \frac{1}{2}$ . It follows that the alignment score  $\mathcal{A}(G^r(\bar{\theta}), G^{bc}(\bar{\theta}))_{t=0}$  converges to a binary random variable with expectation zero in the infinite width limit:

$$\mathcal{A}(G^r(\bar{\theta}), G^{bc}(\bar{\theta}))_{t=0} \rightarrow A = \begin{cases} \text{sgn}(g_{-1} - g_1) \frac{3}{\sqrt{21}} & \text{with prob. } \frac{1}{2}, \\ -\text{sgn}(g_{-1} - g_1) \frac{3}{\sqrt{21}} & \text{with prob. } \frac{1}{2}. \end{cases}$$

**Adam.** We now consider the deterministic version of the Adam optimizer [31], recalled below for completeness. Let  $f(x)$  be a differentiable objective function on  $\mathbb{R}^d$ . The Adam iteration is defined by  $z_n = T_{\gamma, \alpha, \beta}(n, z_{n-1})$  for  $z_n = (x_n, m_n, v_n) \in \mathbb{R}^d \times \mathbb{R}^d \times \mathbb{R}^d$  with  $z_0 = (x_0, 0, 0)$ , where

$$T_{\gamma, \alpha, \beta}(n, z) = \begin{pmatrix} x - \frac{\gamma(1-\alpha^n)^{-1}(\alpha m + (1-\alpha)\nabla f(x))}{\epsilon + (1-\beta^n)^{-1/2}\sqrt{\beta v + (1-\beta)\nabla f(x)^{\odot 2}}} \\ \alpha m + (1-\alpha)\nabla f(x) \\ \beta v + (1-\beta)\nabla f(x)^{\odot 2} \end{pmatrix}.$$

We still consider the gradient conflict at the initialization, since the Adam dynamics is more complicated than the gradient flow one. From [78], we have that starting from  $(x_0, 0, 0) \in \mathbb{R}^{3d}$ , the Adam dynamics at  $t = 0$  satisfies  $\dot{m}(0) \propto \nabla f(x_0)$ ,  $\dot{v}(0) \propto \nabla f(x_0)^{\odot 2}$ , and

$$\dot{x}(0) = -\frac{\nabla f(x_0)}{\epsilon + \sqrt{\nabla f(x_0)^{\odot 2}}} \underset{\epsilon=o(1)}{\approx} -\frac{\nabla f(x_0)}{\sqrt{\nabla f(x_0)^{\odot 2}}},$$

indicating that at early iterations of Adam, the algorithm performance would be similar to the *sign gradient descent* [79]. Back to our problem (D.3), by the above discussion, if we apply Adam to the loss functions  $\mathcal{L}_r(\theta)$  and  $\mathcal{L}_{bc}(\theta)$ , respectively, at the initialization, the normalized weights  $\bar{\theta} = \varepsilon^{-1}\theta$  will be updated along the directions:

$$\frac{\nabla \mathcal{L}_r(\theta)}{\sqrt{\nabla \mathcal{L}_r(\theta)^{\odot 2}}} = \frac{G^r(\bar{\theta})}{\sqrt{G^r(\bar{\theta})^{\odot 2}}} + O(\varepsilon^2), \quad \frac{\nabla \mathcal{L}_{bc}(\theta)}{\sqrt{\nabla \mathcal{L}_{bc}(\theta)^{\odot 2}}} = \frac{G^{bc}(\bar{\theta})}{\sqrt{G^{bc}(\bar{\theta})^{\odot 2}}} + O(\varepsilon^2).$$

Then, by (D.6) and (D.7), one can compute

$$G_{\text{Adam}}^r(\bar{\theta}) = \frac{G^r(\bar{\theta})}{\sqrt{G^r(\bar{\theta})^{\odot 2}}} = \text{sgn}(\bar{\mathbf{a}} \cdot \bar{\mathbf{w}}^{\odot 3}) (\text{sgn}(\bar{\mathbf{w}}), \text{sgn}(\bar{\mathbf{a}})),$$

and

$$G_{\text{Adam}}^{bc}(\bar{\theta}) = \frac{G^{bc}(\bar{\theta})}{\sqrt{G^{bc}(\bar{\theta})^{\odot 2}}} = \text{sgn}(g_{-1} - g_1) (\text{sgn}(\bar{\mathbf{w}}), \text{sgn}(\bar{\mathbf{a}})).$$

It follows that the alignment score is

$$\mathcal{A}(G_{\text{Adam}}^r(\bar{\theta}), G_{\text{Adam}}^{bc}(\bar{\theta})) = \text{sgn}(\bar{\mathbf{a}} \cdot \bar{\mathbf{w}}^{\odot 3}) \text{sgn}(g_{-1} - g_1) = \begin{cases} \text{sgn}(g_{-1} - g_1) & \text{with prob. } \frac{1}{2}, \\ -\text{sgn}(g_{-1} - g_1) & \text{with prob. } \frac{1}{2}, \end{cases}$$

which holds for any two-layer NN with width  $N$ .

**Shampoo and SOAP.** We proceed to consider Shampoo [18], which is a second-order optimizer with Kronecker product preconditioners. For the reader's convenience, we recall the Shampoo iterations for training neural networks. Following the notation in Section 3, let  $W_t, G_t \in \mathbb{R}^{m \times n}$  be the weight matrix and gradient matrix for a layer at time step  $t$ , respectively. Shampoo generates left and right preconditioners:

$$L_t = L_{t-1} + G_t G_t^T, \quad R_t = R_{t-1} + G_t^T G_t,$$

and then updates the weight matrix by

$$W_{t+1} = W_t - \eta L_t^{-1/4} G_t R_t^{-1/4},$$

with step size  $\eta > 0$ . If we disable the accumulation in the preconditioners and set  $L_t = G_t G_t^T$  and  $R_t = G_t^T G_t$ , then the Shampoo optimizer is simplified to

$$W_{t+1} = W_t - \eta \text{Shampoo}(G_t), \quad \text{Shampoo}(G_t) := (G_t G_t^T)^{-1/4} G_t (G_t^T G_t)^{-1/4},$$

with  $\text{Shampoo}(G_t) = U_t V_t^T$ , where  $U_t$  and  $V_t$  are from the reduced singular value decomposition of  $G_t = U_t \Sigma_t V_t^T$ . It is clear that if we apply Shampoo to  $\mathcal{L}_r(\theta)$  or  $\mathcal{L}_{bc}(\theta)$  with the two-layer NN (D.2), then under small initialization Assumption 2, at the initialization, the updates of the normalized weights  $\bar{\theta} = (\bar{\mathbf{a}}, \bar{\mathbf{w}}) = \varepsilon^{-1}\theta$  would be

$$\bar{\mathbf{a}} \leftarrow \bar{\mathbf{a}} - \eta \text{Shampoo}(G_a^{r \text{ or } bc}(\bar{\mathbf{a}}, \bar{\mathbf{w}})), \quad \bar{\mathbf{w}} \leftarrow \bar{\mathbf{w}} - \eta \text{Shampoo}(G_w^{r \text{ or } bc}(\bar{\mathbf{a}}, \bar{\mathbf{w}})).$$

Here  $G_a^{r \text{ or } bc}, G_w^{r \text{ or } bc} \in \mathbb{R}^N$  are given in (D.6) and (D.7). Moreover, note that for any vector  $x \in \mathbb{R}^d$ ,  $\text{Shampoo}(x)$  is simply  $x/\|x\|$ . Therefore, we can compute the (effective) initial Shampoo gradient directions for  $\mathcal{L}_r(\theta)$  and  $\mathcal{L}_{bc}(\theta)$ :

$$G_{\text{Shampoo}}^r(\bar{\theta}) := (\text{Shampoo}(G_a^r(\bar{\theta})), \text{Shampoo}(G_a^r(\bar{\theta}))) = \text{sgn}(\bar{\mathbf{a}} \cdot \bar{\mathbf{w}}^{\odot 3}) \left( \frac{\bar{\mathbf{w}}^{\odot 3}}{\|\bar{\mathbf{w}}^{\odot 3}\|}, \frac{\bar{\mathbf{a}} \odot \bar{\mathbf{w}}^{\odot 2}}{\|\bar{\mathbf{a}} \odot \bar{\mathbf{w}}^{\odot 2}\|} \right).$$

and

$$G_{\text{Shampoo}}^{bc}(\bar{\theta}) := (\text{Shampoo}(G_a^{bc}(\bar{\theta})), \text{Shampoo}(G_a^{bc}(\bar{\theta}))) = \text{sgn}(g_{-1} - g_1) \left( \frac{\bar{\mathbf{w}}}{\|\bar{\mathbf{w}}\|}, \frac{\bar{\mathbf{a}}}{\|\bar{\mathbf{a}}\|} \right).$$

It follows that the alignment score is, as  $N \rightarrow \infty$ ,

$$\mathcal{A}(G_{\text{Shampoo}}^r(\bar{\theta}), G_{\text{Shampoo}}^{bc}(\bar{\theta})) \longrightarrow C_{\text{Shampoo}} \begin{cases} \text{sgn}(g_{-1} - g_1) & \text{with prob. } \frac{1}{2}, \\ -\text{sgn}(g_{-1} - g_1) & \text{with prob. } \frac{1}{2}. \end{cases}$$

We finally consider SOAP. Following the notations in Section 3, if  $G_t$  is a vector, then  $\tilde{G}_t = [1, 0, \dots, 0]^\top$  and  $\text{Adam}(\tilde{G}_t) = \tilde{G}_t$ . We transform this gradient back and obtain  $G_t/\|G_t\|$ . It means that at initialization,

$$\text{Shampoo}(G_a^{r \text{ or } bc}(\bar{\mathbf{a}}, \bar{\mathbf{w}})) = \text{SOAP}(G_a^{r \text{ or } bc}(\bar{\mathbf{a}}, \bar{\mathbf{w}})).$$

Therefore, the initial gradient conflict of SOAP follows from the case of Shampoo. □

## E Additional Lemmas and Proofs

**Lemma 4** ([19], Lemma 1). *Let  $G_1, \dots, G_t \in \mathbb{R}^{m \times n}$  be matrices of rank at most  $r$ . Let  $g_s = \text{vec}(G_s)$  and define  $\hat{H}_t = \epsilon I_{mn} + \sum_{s=1}^t g_s g_s^\top$ . Define  $L_t, R_t$  as above:  $L_t = \epsilon I_m + \sum_{s=1}^t G_s G_s^\top, R_t = \epsilon I_n + \sum_{s=1}^t G_s^\top G_s$ . Then for any  $p, q > 0$  such that  $1/p + 1/q = 1$ , we have  $\hat{H}_t \leq r L_t^{1/p} \otimes R_t^{1/q}$ .*

It follows from the above lemma that for any  $p, q > 0$  with  $1/p + 1/q = 1$ , the full AdaGrad preconditioned gradient  $\hat{H}_t^{-1/2} g_t$  can be approximated by  $(L_t^{1/p} \otimes R_t^{1/q})^{-1/2} g_t = \text{vec}(L_t^{-1/2p} G_t R_t^{-1/2q})$ . In particular, the case of  $p = q = 2$  yields the standard Shampoo update. Moreover, [20] explores the Hessian approximation perspective of Shampoo, showing that the preconditioner in Shampoo is a Kronecker product approximation of the Gauss-Newton component of layerwise Hessian (see Remark 1). Similar arguments will be used below to understand the second-order nature of SOAP.

**Lemma 5** ([20], Corollary 2). *Under the assumption that the reshaping of the Hessian tensor  $H_{GN}$  is rank-1,*

$$\hat{H}_{GN} = (\mathbb{E}[GG^\top] \otimes \mathbb{E}[G^\top G]) / \text{Tr}(\mathbb{E}[GG^\top]).$$

### E.1 Proof of Proposition 1

*Proof.* When  $n = 2$ , we note

$$\begin{aligned} \mathcal{A}(v_1, v_2) &= 2 \left\| \frac{v_1}{\|v_1\|} + \frac{v_2}{\|v_2\|} \right\|^2 - 1 \\ &= \frac{1}{2} \left( \left\| \frac{v_1}{\|v_1\|} \right\|^2 + 2 \frac{v_1 \cdot v_2}{\|v_1\| \|v_2\|} + \left\| \frac{v_2}{\|v_2\|} \right\|^2 \right) - 1 \\ &= \frac{1}{2} (1 + 2 \cos(v_1, v_2) + 1) - 1 = \cos(v_1, v_2). \end{aligned} \quad \square$$

### E.2 Proof of Lemma 1

*Proof.* By Taylor expansion, the gradient at step  $t + 1$  can be expressed as:

$$\begin{aligned} g_{t+1} &= g_t + H(\theta_t)(\theta_{t+1} - \theta_t) + O(\|\theta_{t+1} - \theta_t\|^2) \\ &= g_t - \eta H(\theta_t) H^{-1}(\theta_t) g_t + O(\eta^2 \|g_t\|^2) \\ &= (1 - \eta) g_t + O(\eta^2 \|g_t\|^2). \end{aligned}$$

Then, it is easy to compute

$$\begin{aligned}
\mathcal{A}(g_t, g_{t+1}) &= \frac{g_{t+1} \cdot g_t}{\|g_{t+1}\| \|g_t\|} \\
&= \frac{(1-\eta)\|g_t\|^2 + O(\eta^2\|g_t\|^3)}{\|g_{t+1}\| \|g_t\|} \\
&= \frac{(1-\eta)\|g_t\|^2 + O(\eta^2\|g_t\|^3)}{((1-\eta)\|g_t\| + O(\eta^2\|g_t\|^2))\|g_t\|} \\
&= \frac{1-\eta + O(\eta^2\|g_t\|)}{1-\eta + O(\eta^2\|g_t\|)} \\
&= 1 + O(\eta^2\|g_t\|). \quad \square
\end{aligned}$$

### E.3 Proof of Proposition 2

*Proof.* For each layer-weight matrix  $W$  with  $w = \text{vec}(W)$ , the initial, boundary and PDE losses can be approximated via second-order Taylor expansion around  $w^*$ :

$$\begin{aligned}
\mathcal{L}_{ic}(W) &\approx \mathcal{L}_{ic}(w^*) + \frac{1}{2}(w - w^*)^T H_{ic}(w - w^*), \\
\mathcal{L}_{bc}(W) &\approx \mathcal{L}_{bc}(w^*) + \frac{1}{2}(w - w^*)^T H_{bc}(w - w^*), \\
\mathcal{L}_r(w) &\approx \mathcal{L}_r(w^*) + \frac{1}{2}(w - w^*)^T H_r(w - w^*),
\end{aligned}$$

where  $H_b$  and  $H_r$  denote the Hessians of  $\mathcal{L}_b$  and  $\mathcal{L}_r$  at  $w^*$ , respectively. Taking gradients with respect  $w$  we have

$$g_{ic} \approx H_{ic}(w - w^*), \quad g_{bc} \approx H_{bc}(w - w^*), \quad g_r \approx H_r(w - w^*).$$

Recall from Theorem 1, SOAP approximates  $H^{-1}$  as the preconditioner. When applying SOAP optimizers to  $\mathcal{L}_{ic}$ ,  $\mathcal{L}_{bc}$  and  $\mathcal{L}_r$  separately, we obtain:

$$\begin{aligned}
\mathcal{A}(\text{Soap}(G_{ic}), \text{Soap}(G_{bc}), \text{Soap}(G_r)) &\approx \mathcal{A}(H_{ic}^{-1}g_{ic}, H_{bc}^{-1}g_{bc}, H_r^{-1}g_r) \\
&\approx \mathcal{A}(H_{ic}^{-1}H_{ic}(w - w^*), H_{bc}^{-1}H_{bc}(w - w^*), H_r^{-1}H_r(w - w^*)) \approx 1. \quad \square
\end{aligned}$$

## F Experimental Details

### F.1 Architectures

This section outlines the network architectures employed in our work, along with the enhancements introduced to improve their performance.

**Modified MLP.** The modified MLP architecture is proposed by [7], which has been extensively used in the literature [10, 32, 64, 80–82] due to its improved capability in learning complex PDE solutions. The network processes input coordinates through two parallel encoders:

$$\mathbf{U} = \sigma(\mathbf{W}_1 \mathbf{x} + \mathbf{b}_1), \quad \mathbf{V} = \sigma(\mathbf{W}_2 \mathbf{x} + \mathbf{b}_2). \quad (\text{F.1})$$

Then, for  $l = 1, 2, \dots, L$ , the forward pass is defined as:

$$\mathbf{f}^{(l)}(\mathbf{x}) = \mathbf{W}^{(l)} \cdot \mathbf{g}^{(l-1)}(\mathbf{x}) + \mathbf{b}^{(l)}, \quad (\text{F.2})$$

$$\mathbf{g}^{(l)}(\mathbf{x}) = \sigma(\mathbf{f}_\theta^{(l)}(\mathbf{x})) \odot \mathbf{U} + \left(1 - \sigma(\mathbf{f}_\theta^{(l)}(\mathbf{x}))\right) \odot \mathbf{V} \quad (\text{F.3})$$

The final network output is given by

$$\mathbf{f}_\theta(\mathbf{x}) = \mathbf{W}^{(L+1)} \cdot \mathbf{g}^{(L)}(\mathbf{x}) + \mathbf{b}^{(L+1)}. \quad (\text{F.4})$$

where  $\sigma$  is a nonlinear activation function,  $\odot$  denotes element-wise multiplication, and the trainable parameters are:

$$\theta = \left\{ \mathbf{W}_1, \mathbf{b}_1, \mathbf{W}_2, \mathbf{b}_2, \left( \mathbf{W}^{(l)}, \mathbf{b}^{(l)} \right)_{l=1}^{L+1} \right\}. \quad (\text{F.5})$$

This architecture extends the standard MLP by incorporating dual input encoders and merging their features through point-wise multiplication at each hidden layer. While computationally more demanding, this modification demonstrates superior performance in minimizing PDE residuals compared to standard MLPs.

**PirateNet.** PirateNet is proposed by [28], which aims to enable stable and efficient training of deep PINN models. The architecture first transforms input coordinates  $\mathbf{x}$  into a high-dimensional feature space using random Fourier features [83]:

$$\Phi(\mathbf{x}) = \begin{bmatrix} \cos(\mathbf{B}\mathbf{x}) \\ \sin(\mathbf{B}\mathbf{x}) \end{bmatrix},$$

where  $\mathbf{B} \in \mathbb{R}^{m \times d}$  has entries sampled i.i.d. from  $\mathcal{N}(0, s^2)$  with user-specified  $s > 0$ . This embedding mitigates spectral bias in PINNs by improving the eigenfunction frequency of the Neural Tangent Kernel, enabling better learning of high-frequency components and multiscale features [84].

The embedded coordinates are processed through two dense layers that act as gates:

$$\mathbf{U} = \sigma(\mathbf{W}_1\Phi(\mathbf{x}) + \mathbf{b}_1), \quad \mathbf{V} = \sigma(\mathbf{W}_2\Phi(\mathbf{x}) + \mathbf{b}_2),$$

where  $\sigma$  is a point-wise activation function. This gating mechanism is essentially the same as in modified MLP.

Let  $\mathbf{x}^{(1)} = \Phi(\mathbf{x})$  and  $\mathbf{x}^{(l)}$  be the input to the  $l$ -th block ( $1 \leq l \leq L$ ). Each block performs:

$$\mathbf{f}^{(l)} = \sigma(\mathbf{W}_1^{(l)}\mathbf{x}^{(l)} + \mathbf{b}_1^{(l)}), \quad (\text{F.6})$$

$$\mathbf{z}_1^{(l)} = \mathbf{f}^{(l)} \odot \mathbf{U} + (1 - \mathbf{f}^{(l)}) \odot \mathbf{V}, \quad (\text{F.7})$$

$$\mathbf{g}^{(l)} = \sigma(\mathbf{W}_2^{(l)}\mathbf{z}_1^{(l)} + \mathbf{b}_2^{(l)}), \quad (\text{F.8})$$

$$\mathbf{z}_2^{(l)} = \mathbf{g}^{(l)} \odot \mathbf{U} + (1 - \mathbf{g}^{(l)}) \odot \mathbf{V}, \quad (\text{F.9})$$

$$\mathbf{h}^{(l)} = \sigma(\mathbf{W}_3^{(l)}\mathbf{z}_2^{(l)} + \mathbf{b}_3^{(l)}), \quad (\text{F.10})$$

$$\mathbf{x}^{(l+1)} = \alpha^{(l)}\mathbf{h}^{(l)} + (1 - \alpha^{(l)})\mathbf{x}^{(l)}, \quad (\text{F.11})$$

Each block comprises three dense layers with dual gating operations and an adaptive residual connection. The trainable  $\alpha^{(l)}$  parameters control block nonlinearity:  $\alpha^{(l)} = 0$  yields an identity mapping, while  $\alpha^{(l)} = 1$  produces fully nonlinear transformation.

The final output of a PirateNet of  $L$  residual blocks is given by

$$\mathbf{u}_\theta = \mathbf{W}^{(L+1)}\mathbf{x}^{(L)}. \quad (\text{F.12})$$

Importantly, we initialize  $\alpha^{(l)} = 0$ , making the initial output a linear combination of first-layer embeddings. This initialization strategy mitigates training difficulties in deep networks by starting with effectively shallow architecture and gradually increasing depth through learned  $\alpha$  values. Additionally, the linear structure at initialization enables direct integration of prior solution data through least squares fitting:

$$\min_{\mathbf{W}} \|\mathbf{W}\Phi - \mathbf{Y}\|_2^2, \quad (\text{F.13})$$

where  $\mathbf{Y}$  represents available measurements. This approach provides an optimal initial guess based on various data sources, including experimental measurements, boundary conditions, or linearized PDE solutions.

**Exact imposition of periodic boundary conditions.** We adopt the approach of [30] to enforce periodic boundary conditions as hard constraints, improving both training convergence and accuracy. Consider a one-dimensional periodic function with period  $P$  satisfying:

$$u^{(l)}(a) = u^{(l)}(a + P), \quad l = 0, 1, 2, \dots \quad (\text{F.14})$$

We construct a Fourier feature embedding:

$$\mathbf{v}(x) = (\cos(\omega x), \sin(\omega x)), \quad (\text{F.15})$$

where  $\omega = \frac{2\pi}{L}$ . Any network  $u_\theta(v(x))$  using this embedding inherently satisfies the periodic boundary condition.

The same idea can be directly extended to higher-dimensional domains. For two-dimensional domains, the periodicity constraints are:

$$\frac{\partial^l}{\partial x^l} u(a, y) = \frac{\partial^l}{\partial x^l} u(a + P_x, y), \quad y \in [b, b + P_y], \quad (\text{F.16})$$

$$\frac{\partial^l}{\partial y^l} u(x, a) = \frac{\partial^l}{\partial y^l} u(x, b + P_y), \quad x \in [a, a + P_x], \quad (\text{F.17})$$

for  $l = 0, 1, 2, \dots$ , where  $P_x$  and  $P_y$  are the periods in the  $x$  and  $y$  directions, respectively. Similarly, these constraints are encoded using the embedding:

$$\mathbf{v}(x, y) = [\cos(\omega_x x), \sin(\omega_x x), \cos(\omega_y y), \sin(\omega_y y)] \quad (\text{F.18})$$

with  $w_x = \frac{2\pi}{P_x}, w_y = \frac{2\pi}{P_y}$ .

For time-dependent problems, we concatenate time coordinates  $t$  with spatial embeddings:  $u_\theta([t, \mathbf{v}(x)])$  or  $u_\theta([t, \mathbf{v}(x, y)])$ .

**Random weight factorization.** We implement random weight factorization (RWF) [29] to enhance PINN performance. RWF decomposes each neuron's weight vector as:

$$\mathbf{w}^{(k,l)} = s^{(k,l)} \cdot \mathbf{v}^{(k,l)}, \quad (\text{F.19})$$

where  $k = 1, \dots, d_l, l = 1, \dots, L + 1$ ,  $\mathbf{w}^{(k,l)} \in \mathbb{R}^{d_{l-1}}$  is the  $k$ -th row of weight matrix  $\mathbf{W}^{(l)}$ ,  $s^{(k,l)} \in \mathbb{R}$  is a trainable scale factor, and  $\mathbf{v}^{(k,l)} \in \mathbb{R}^{d_{l-1}}$ . This factorization can be expressed in matrix form as:

$$\mathbf{W}^{(l)} = \text{diag}(\mathbf{s}^{(l)}) \cdot \mathbf{V}^{(l)}, \quad l = 1, 2, \dots, L + 1 \quad (\text{F.20})$$

with  $\mathbf{s}^{(l)} \in \mathbb{R}^{d_l}$ .

Implementation involves: (1) initializing MLP parameters using the Glorot scheme [85], (2) initializing scale vectors  $\exp(s)$  where  $s \sim \mathcal{N}(\mu, \sigma \mathbf{I})$ , (3) factorizing each weight matrix as  $\mathbf{W} = \text{diag}(\exp(\mathbf{s})) \cdot \mathbf{V}$ , and (4) optimizing parameters  $\mathbf{s}, \mathbf{V}$  directly. We employ exponential parameterization following Weight Normalization [86] to ensure non-zero scale factors across varied magnitudes. We recommend  $\mu = 0.5$  or  $1$  and  $\sigma = 0.1$ , as these values consistently improve convergence and accuracy while avoiding the instability of larger values or the diminished effect of smaller ones.

## F.2 Training pipeline

This section details the methodologies and strategies used to train PINN models.

**Causal training.** Recent work by [32] shows that PINNs may violate temporal causality when solving time-dependent PDEs, as they tend to minimize residuals at later times before correctly solving earlier times. To address this, we introduce a causality-aware training approach. We partition the temporal domain into  $M$  equal segments and denote the PDE residual loss within the  $i$ -th segment as  $\mathcal{L}_r^i$ . The modified residual loss becomes:

$$\mathcal{L}_r(\theta) = \frac{1}{M} \sum_{i=1}^M w_i \mathcal{L}_r^i(\theta). \quad (\text{F.21})$$

We compute the temporal weights as

$$w_i = \exp\left(-\epsilon \sum_{k=1}^{i-1} \mathcal{L}_r^k(\theta)\right), \quad \text{for } i = 2, 3, \dots, M. \quad (\text{F.22})$$

Then,

$$\mathcal{L}_r(\theta) = \frac{1}{M} \sum_{i=1}^M \exp\left(-\epsilon \sum_{k=1}^{i-1} \mathcal{L}_r^k(\theta)\right) \mathcal{L}_r^i(\theta). \quad (\text{F.23})$$

The weight  $w_i$  decreases exponentially with the cumulative residual loss from previous time steps. This ensures that  $\mathcal{L}_r^i(\theta)$  is minimized only after previous residuals  $\{\mathcal{L}_r^k(\theta)\}_{k=1}^{i-1}$  become sufficiently small, enforcing temporal causality in the optimization process.

The causality parameter  $\epsilon$  requires careful tuning: small values may insufficiently enforce causality, while large values can create optimization difficulties by requiring extremely small early-time residuals before later times are considered. We recommend selecting a moderate  $\epsilon$  that allows all temporal weights to converge to 1 by training completion, reducing it if necessary.

**Learning rate annealing.** A key challenge in training PINNs is handling multi-scale losses from PDE residuals that cannot be normalized during preprocessing process. While loss weighting can address this, manual weight selection is impractical due to their problem-dependent nature and the absence of validation data for hyperparameter tuning in PDE solving.

We implement a self-adaptive learning rate annealing algorithm [7] that automatically balances the weighted loss:

$$\mathcal{L}(\theta) = \lambda_{ic}\mathcal{L}_{ic}(\theta) + \lambda_{bc}\mathcal{L}_{bc}(\theta) + \lambda_r\mathcal{L}_r(\theta), \quad (\text{F.24})$$

The global weights are computed as:

$$\hat{\lambda}_{ic} = \frac{\|\nabla_{\theta}\mathcal{L}_{ic}(\theta)\| + \|\nabla_{\theta}\mathcal{L}_{bc}(\theta)\| + \|\nabla_{\theta}\mathcal{L}_r(\theta)\|}{\|\nabla_{\theta}\mathcal{L}_{ic}(\theta)\|}, \quad (\text{F.25})$$

$$\hat{\lambda}_{bc} = \frac{\|\nabla_{\theta}\mathcal{L}_{ic}(\theta)\| + \|\nabla_{\theta}\mathcal{L}_{bc}(\theta)\| + \|\nabla_{\theta}\mathcal{L}_r(\theta)\|}{\|\nabla_{\theta}\mathcal{L}_{bc}(\theta)\|}, \quad (\text{F.26})$$

$$\hat{\lambda}_r = \frac{\|\nabla_{\theta}\mathcal{L}_{ic}(\theta)\| + \|\nabla_{\theta}\mathcal{L}_{bc}(\theta)\| + \|\nabla_{\theta}\mathcal{L}_r(\theta)\|}{\|\nabla_{\theta}\mathcal{L}_r(\theta)\|}, \quad (\text{F.27})$$

where  $\|\cdot\|$  denotes the  $L^2$  norm. Then we obtain

$$\|\hat{\lambda}_{ic}\nabla_{\theta}\mathcal{L}_{ic}(\theta)\| = \|\hat{\lambda}_{bc}\nabla_{\theta}\mathcal{L}_{bc}(\theta)\| = \|\hat{\lambda}_r\nabla_{\theta}\mathcal{L}_r(\theta)\| = \|\nabla_{\theta}\mathcal{L}_{ic}(\theta)\| + \|\nabla_{\theta}\mathcal{L}_{bc}(\theta)\| + \|\nabla_{\theta}\mathcal{L}_r(\theta)\|. \quad (\text{F.28})$$

This formulation equalizes the gradient norms of weighted losses, preventing bias toward any particular term during training. The weights are updated as running averages of their previous values, stabilizing stochastic gradient descent. Updates occur at user-specified intervals (typically every 100-1000 iterations), leading to minimal computational overhead.

**Curriculum training and time-marching.** Despite the improvements described above, PINNs still face challenges in complex domains requiring high accuracy, such as chaotic systems like high Reynolds number Navier-Stokes equations where error accumulation can cause trajectory divergence. We address these challenges using curriculum training [33], which decomposes the optimization into more manageable sub-tasks.

An effective approach we employ is the curriculum training strategy introduced by [33]. The core idea involves decomposing the entire optimization task for PINNs into a sequence of more manageable sub-tasks. In this work, we mainly focus on integrating this strategy into our training pipeline for solving time-dependent PDEs and singular perturbation problems.

For time-dependent PDEs, we implement temporal domain decomposition: the time domain is divided into smaller intervals. After the first window, initial conditions for subsequent windows are set using predictions from the final step of the previous window. This approach reduces the difficulty of the optimization task of learning full system dynamics, though at an increased computational cost due to per-window model retraining.

While we also partition the temporal domain to compute causal weights within each window, this differs from the time-marching strategy. Both techniques promote learning solutions sequentially along the time axis to respect causality, but causal weighting complements rather than replaces time-marching, as causality violations may still occur within individual time windows.

### F.3 Data Generation

We generate our reference dataset using two numerical packages: Chebfun [87] in MATLAB and Incompressible-NavierStokes [88] in Julia. The data generation process employs a time step of  $dt = 10^{-4}$ , followed by temporal downsampling to construct the final dataset. Table 3 summarizes the PDE parameters and dataset details.

### F.4 Hyper-parameters

The complete set of hyperparameters is detailed in Table 4, largely following the configurations established in [27, 28]. The decay step is adapted for each benchmark to ensure the learning rate reaches a sufficiently small value (e.g.,  $10^{-7}$ ) by the end of training. The number of time windows is determined empirically based on problem complexity, with fine-tuning guided by the loss convergence behavior during preliminary experiments.

### F.5 Computational Cost

Our implementation is based on JAX-PI [27] and we conducted all experiments on a single NVIDIA A6000 GPU, with detailed runtime benchmarks reported in Table 5.

Table 3: Parameter settings and numerical configurations for generating the reference solution across PDE benchmarks.

PDE	Parameter	Package	Resolution
<b>Wave</b>	$c = 4$	N/A	$200 \times 128$
<b>Burgers</b>	$\nu = 0.01 \pi$	Chebfun	$200 \times 512$
<b>AC</b>	$\epsilon = 10^{-4}, a = 5$	Chebfun	$200 \times 512$
<b>KdV</b>	$\eta = 1, \mu = 0.022$	Chebfun	$200 \times 512$
<b>KS</b>	$\alpha = 100/16, \beta = 100/16^2, \gamma = 100/16^4$	Chebfun	$250 \times 512$
<b>GS</b>	$\epsilon_1 = 0.2, \epsilon_2 = 0.1, b_1 = 40, b_2 = 100, c_1 = c_2 = 1,000$	Chebfun	$100 \times 200 \times 200$
<b>GL</b>	$\epsilon = 0.004, \mu = 10, \gamma = 10 + 15i$	Chebfun	$100 \times 200 \times 200$
<b>LDC</b>	$\text{Re}=5 \times 10^3$	IncompressibleNavierStokes	$128 \times 128$
<b>KF</b>	$\text{Re}=10^4$	IncompressibleNavierStokes	$50 \times 512 \times 512$
<b>RT</b>	$\text{Ra}=10^6, \text{Pr} = 0.71$	IncompressibleNavierStokes	$40 \times 100 \times 200$

Table 4: *Hyperparameter configurations for benchmark PDEs.* Hyperparameter settings used to reproduce our experimental results. The backbone architecture is PirateNet, where Depth indicates the number of adaptive residual blocks, and Width denotes the number of neurons per hidden layer. RFF and RWF represent Random Fourier Features and Random Weight Factorization, respectively.

Parameter	Wave	Burgers	AC	KdV	KS	GS	GL	LDC	KF	RT
<b>Architecture</b>										
Depth	3	3	3	3	3	3	3	4	3	3
Width	256	256	256	256	256	256	256	256	384	384
Activation	Tanh	Tanh	Tanh	Tanh	Tanh	Swish	Swish	Tanh	Tanh	Tanh
RFF scale	10.0	2.0	2.0	2.0	2.0	2.0	2.0	10.0	2.0	2.0
RWF					$\mu=1.0, \sigma=0.1$					
<b>Learning rate schedule</b>										
Initial learning rate					$10^{-3}$					
Decay rate					0.9					
Decay steps	$2 \times 10^3$	$2 \times 10^3$	$5 \times 10^3$	$2 \times 10^3$	$2 \times 10^3$	$2 \times 10^3$	$2 \times 10^3$	$2 \times 10^3$	$2 \times 10^3$	$2 \times 10^3$
Warmup steps					$5 \times 10^3$					
<b>Training</b>										
Iters (per time window)	$10^5$	$10^5$	$3 \times 10^5$	$10^5$	$10^5$	$10^5$	$10^5$	$2 \times 10^5$	$2 \times 10^4$	$10^5$
Batch size					8,192					
# Time windows	1	1	1	1	10	10	5	N / A	25	4
<b>Weighting Scheme</b>					Grad Norm					
<b>Causal weighting</b>										
Tolerance	1.0	1.0	1.0	1.0	1.0	1.0	1.0	N / A	1.0	1.0
# Chunks	16	16	16	16	16	16	16	N / A	16	16

Table 5: Computational runtime (in hours) comparison of different methods across various PDEs. All experiments are performed on an Nvidia A6000 GPU, reporting the total training time needed to achieve convergence using PINNs with Adam and SOAP, respectively

Benchmark	Adam	SOAP
Wave	2.80	4.35
Burgers	1.18	4.05
Allen-Cahn	1.48	5.83
Korteweg–De Vries	1.61	3.90
Kuramoto-Sivashinsky	19.51	34.16
Grey-Scott	19.52	40.01
Ginzburg-Landau	15.98	23.75
Lid-driven cavity (Re = $5 \times 10^3$ )	5.67	8.25
Kolmogorov flow (Re = $10^4$ )	9.56	11.00
Rayleigh-Taylor instability (Pr = 0.71, Ra = $10^6$ )	20.23	21.73

## F.6 Benchmarks

**Wave equation.** We consider a one-dimensional wave equation in the domain  $\Omega = [0, 1] \times [0, 1]$  taking the form

$$\begin{aligned} u_{tt}(x, t) - 4u_{xx}(x, t) &= 0, & (x, t) \in (0, 1) \times (0, 1), \\ u(0, t) = u(1, t) &= 0, & t \in [0, 1], \\ u(x, 0) &= \sin(\pi x) + \frac{1}{2} \sin(4\pi x), & x \in [0, 1], \\ u_t(x, 0) &= 0, & x \in [0, 1]. \end{aligned}$$

where  $u$  represents the wave amplitude, and  $c$  is the wave propagation speed, determined by the medium’s physical properties.

By d’Alembert’s formula, the solution  $u(x, t)$  is given by

$$u(x, t) = \sin(\pi x) \cos(2\pi t) + \frac{1}{2} \sin(4\pi x) \cos(8\pi t).$$

**Burgers equation.** The 1D Burgers equation is defined as:

$$u_t + uu_x = \nu u_{xx},$$

where  $u$  represents the velocity field, and  $\nu$  is the kinematic viscosity coefficient controlling the diffusion strength. Here we set  $(x, t) \in \Omega = [-1, 1] \times [0, 1]$ , with initial and boundary conditions:

$$\begin{aligned} u(x, 0) &= -\sin(\pi x), \\ u(-1, t) = u(1, t) &= 0, \end{aligned}$$

and viscosity parameter  $\nu = 0.01/\pi$ .

**Allen-Cahn equation.** We investigate the one-dimensional Allen-Cahn equation with periodic boundary conditions:

$$\begin{aligned} u_t - 0.0001u_{xx} + 5u^3 - 5u &= 0, & t \in [0, 1], x \in [-1, 1], \\ u(0, x) &= x^2 \cos(\pi x), \\ u(t, -1) = u(t, 1), & u_x(t, -1) = u_x(t, 1). \end{aligned}$$

where  $u$  represents the order parameter (e.g., concentration difference between two phases),  $\epsilon$  controls the interfacial width,  $a$  is the reaction rate coefficient, and the term  $(u - u^3)$  drives the phase separation.

It is worth noting that this benchmark has been extensively used to validate the effectiveness of PINNs methodologies. In Table 6, we compare the test errors across different PINNs advancements, demonstrating that our approach achieves state-of-the-art performance with an improvement of up to one order of magnitude in accuracy.

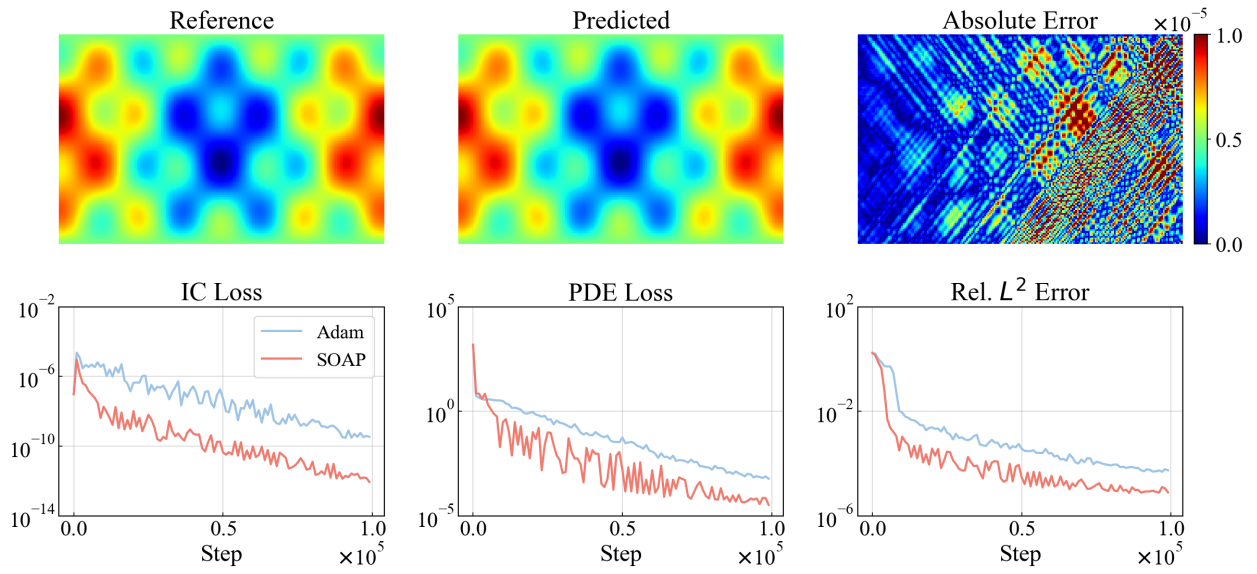


Figure 5: *Wave equation*. Top: Comparison between the reference solution and the model predictions. Bottom: Training loss and test error trajectories for the Adam and SOAP optimizers.

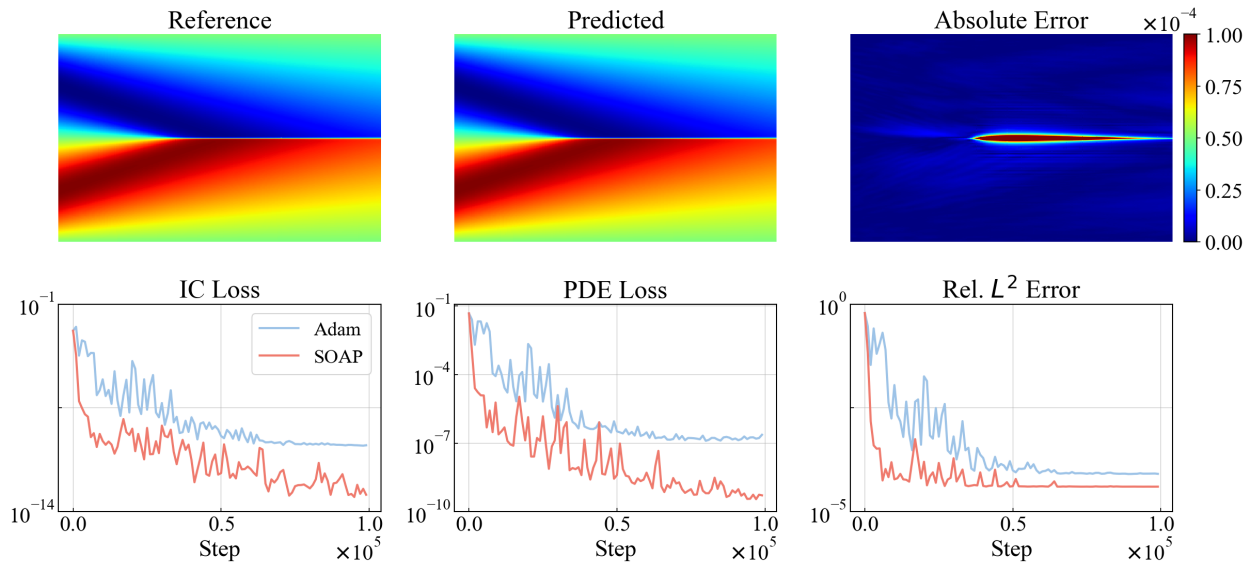


Figure 6: *Burgers' equation*. Top: Comparison between the reference solution and model predictions. Bottom: Training loss and test error trajectories for the Adam and SOAP optimizers.

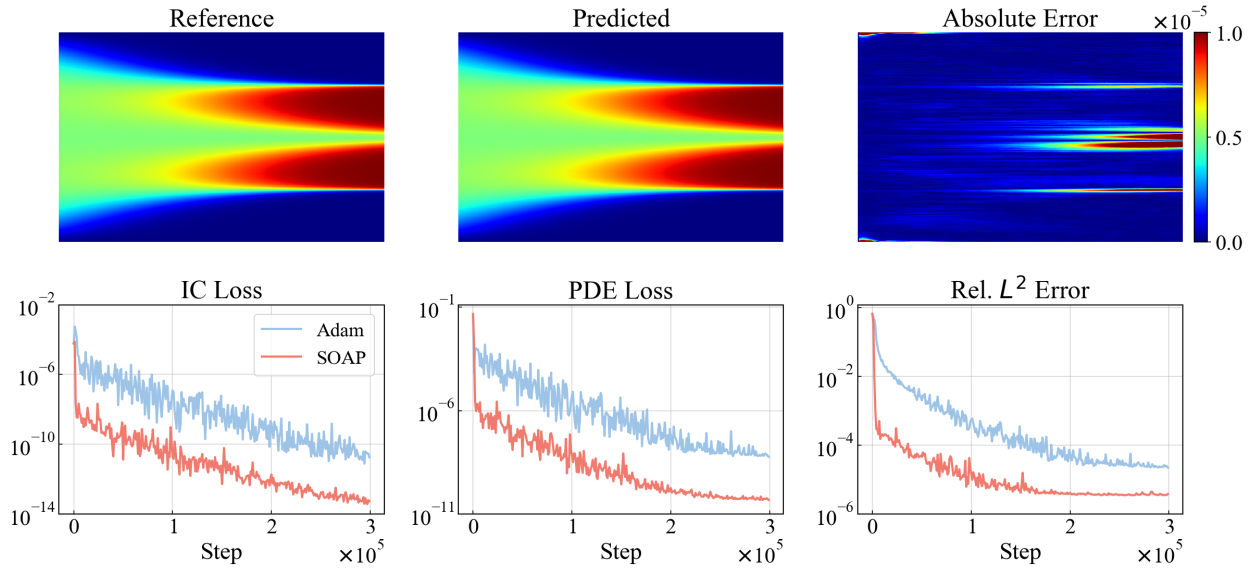


Figure 7: *Allen-Cahn equation*. Top: Comparison between the reference solution and model predictions. Bottom: Training loss and test error trajectories for the Adam and SOAP optimizers.

Table 6: *Allen-Cahn equation*: Relative  $L^2$  test errors obtained by different PINNs variants.

Method	Relative $L^2$ error
Original formulation of Raissi <i>et al.</i> [5]	$4.98 \times 10^{-1}$
Adaptive time sampling [67]	$2.33 \times 10^{-2}$
Self-attention [89]	$2.10 \times 10^{-2}$
Time marching [90]	$1.68 \times 10^{-2}$
Causal training [32]	$1.39 \times 10^{-4}$
Dirac delta function causal training [91]	$6.29 \times 10^{-5}$
JAX-PI [27]	$5.37 \times 10^{-5}$
RBA-PINNs [80]	$4.55 \times 10^{-5}$
PirateNet [28]	$2.24 \times 10^{-5}$
BRDR-PINNs [10]	$1.45 \times 10^{-5}$
<b>Ours</b>	<b><math>3.48 \times 10^{-6}</math></b>

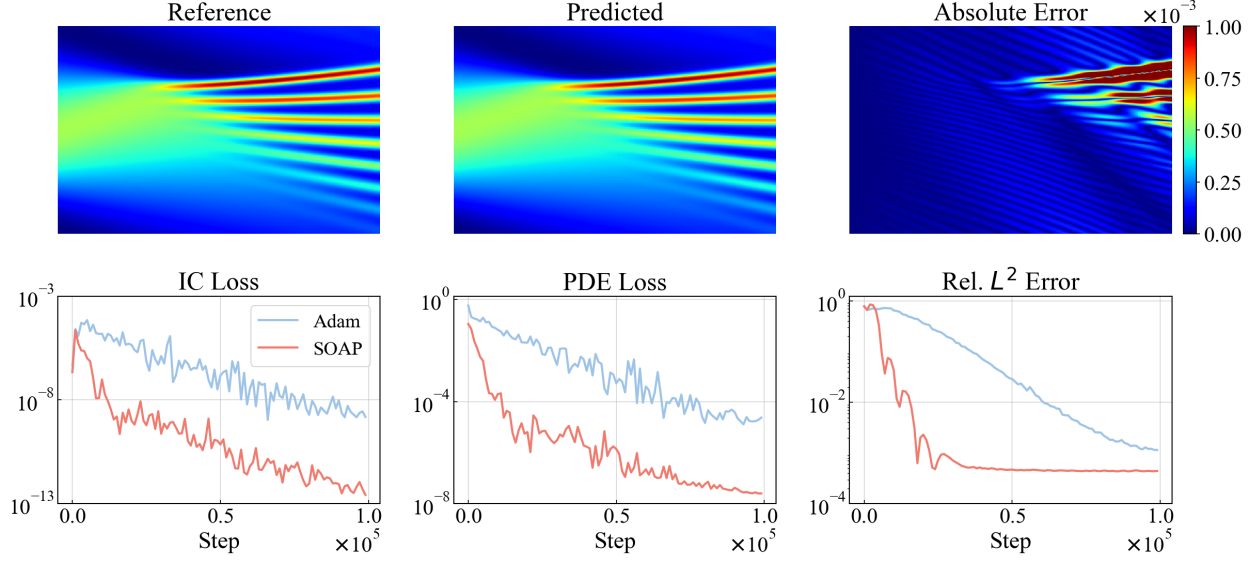


Figure 8: *Korteweg-De Vries equation*. Top: Comparison between the reference solution and model predictions. Bottom: Training loss and test error trajectories for the Adam and SOAP optimizers.

**Korteweg-De Vries equation.** The one-dimensional KdV equation is expressed as follows:

$$\begin{aligned} u_t + \eta uu_x + \mu^2 u_{xxx} &= 0, \quad t \in (0, 1), \quad x \in (-1, 1), \\ u(x, 0) &= \cos(\pi x), \\ u(t, -1) &= u(t, 1), \end{aligned}$$

where  $u$  represents the wave amplitude or water surface elevation, and  $\eta$  governs the strength of the nonlinearity, while  $\mu$  controls the dispersion level. Under the KdV dynamics, this initial wave evolves into a series of solitary-type waves. For our study, we adopt the classical parameters of the KdV equation, setting  $\eta = 1$  and  $\mu = 0.022$  [92].

**Kuramoto-Sivashinsky equation.** The one-dimensional equation takes the form:

$$\begin{aligned} u_t + \alpha uu_x + \beta u_{xx} + \gamma u_{xxxx} &= 0, \quad t \in [0, T], x \in [0, 2\pi], \\ u(0, x) &= u_0(x), \end{aligned}$$

where  $u$  represents the height of a thin film or flame front. This equation arises in various physical contexts, including flame front propagation, thin film flows, and plasma instabilities.

In this example, we take  $T = 0.8$ ,  $\alpha = 100/16$ ,  $\beta = 100/16^2$ ,  $\gamma = 100/16^4$  and  $u_0(x) = \cos(x)(1 + \sin(x))$ .

**Grey-Scott equation.** The system is described by the following coupled PDEs:

$$\begin{aligned} u_t &= \epsilon_1 \Delta u + b_1(1 - u) - c_1 uv^2, \quad t \in (0, 2), (x, y) \in (-1, 1)^2, \\ v_t &= \epsilon_2 \Delta v - b_2 v + c_2 uv^2, \quad t \in (0, 2), (x, y) \in (-1, 1)^2, \end{aligned}$$

With periodic boundary conditions, the initial conditions are:

$$\begin{aligned} u_0(x, y) &= 1 - \exp(-10((x + 0.05)^2 + (y + 0.02)^2)), \\ v_0(x, y) &= 1 - \exp(-10((x - 0.05)^2 + (y - 0.02)^2)). \end{aligned}$$

where  $u$  and  $v$  represent activator and inhibitor concentrations respectively,  $\epsilon_1$  and  $\epsilon_2$  are diffusion coefficients, and  $(b_1, b_2, c_1, c_2)$  control reaction kinetics. This system generates diverse spatial patterns including spots and stripes.

We set parameters  $\epsilon_1 = 0.2$ ,  $\epsilon_2 = 0.1$ ,  $b_1 = 40$ ,  $b_2 = 100$ , and  $c_1 = c_2 = 1,000$ , which generates characteristic pattern formations. Due to the similar behavior of  $u$  and  $v$ , we report only the relative  $L^2$  error of  $u$  in Table 1.

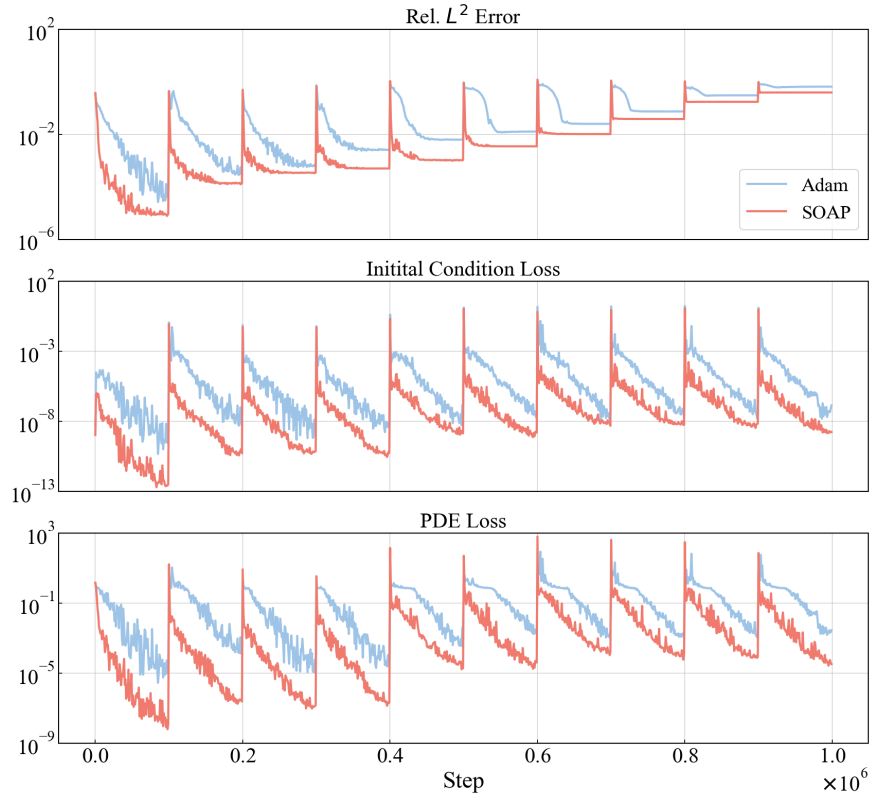


Figure 9: Kuramoto-Sivashinsky equation. Training loss and test error trajectories for the Adam and SOAP optimizers.

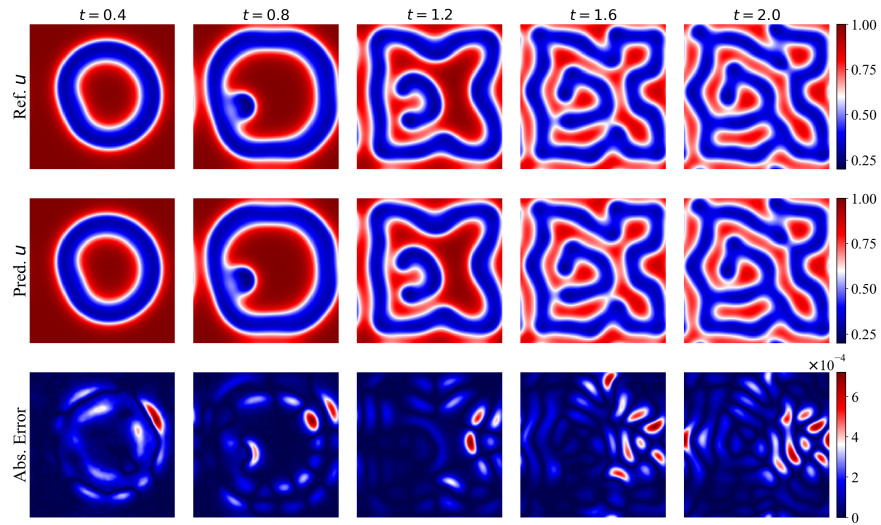


Figure 10: Grey-Scott equation. Comparison between reference solution and model predictions.

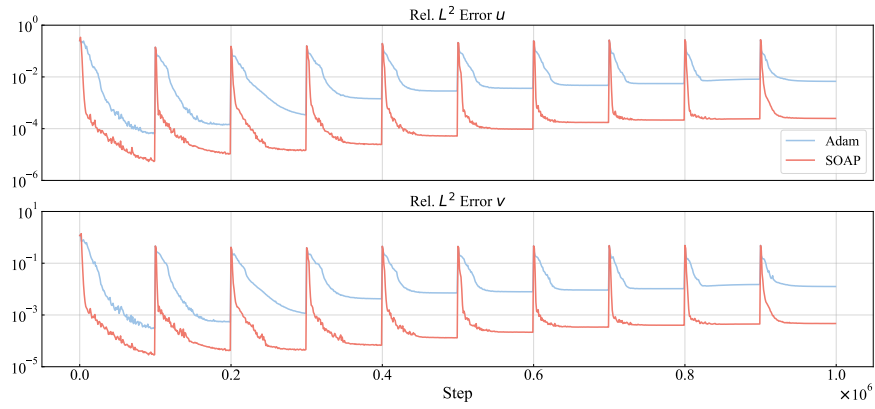


Figure 11: *Grey-Scott equation*. Test error trajectories for the Adam and SOAP optimizers.

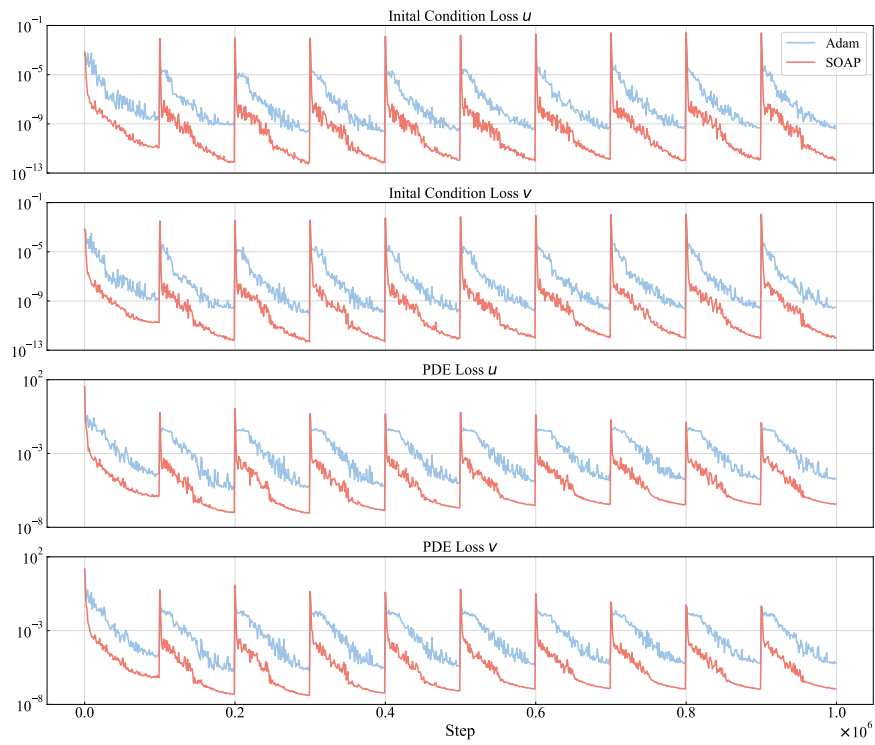


Figure 12: *Grey-Scott equation*. Training loss and test error trajectories for the Adam and SOAP optimizers.

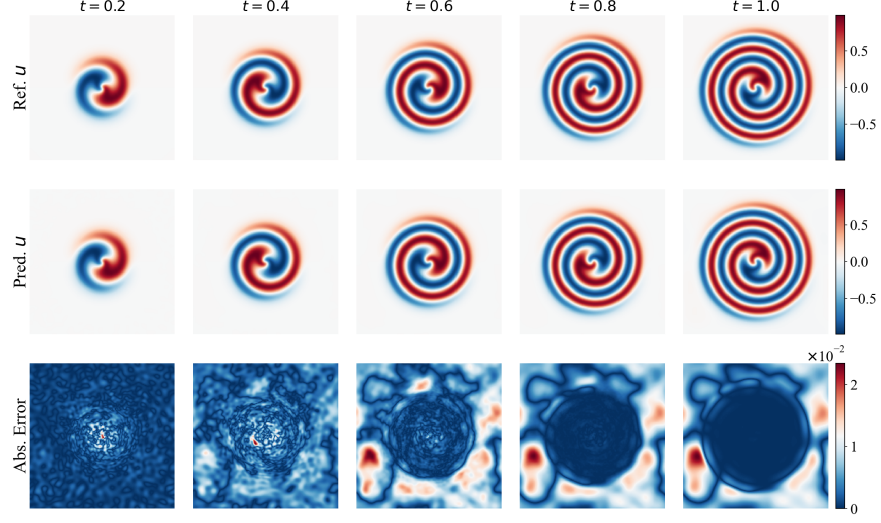


Figure 13: *Ginzburg-Landau equation*. Comparison between the reference solution and model predictions.

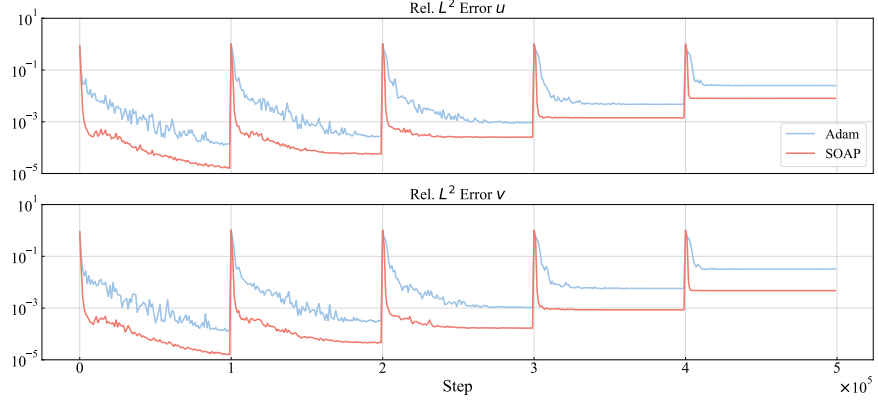


Figure 14: *Ginzburg-Landau equation*. Test error trajectories for the Adam and SOAP optimizers.

**Ginzburg-Landau equation.** The complex Ginzburg-Landau equation in 2D takes the form

$$\frac{\partial A}{\partial t} = \epsilon \Delta A + \mu A - \gamma A |A|^2, \quad t \in (0, 1), (x, y) \in (-1, 1)^2,$$

with periodic boundary conditions, an initial condition

$$A_0(x, y) = (10y + 10ix) \exp(-0.01(2500x^2 + 2500y^2)),$$

where  $A$  is the complex amplitude representing the envelope of oscillations,  $\epsilon$  represents the diffusion coefficient,  $\mu$  is the linear growth rate, and  $\gamma$  controls the nonlinear saturation. For this example, we set  $\epsilon = 0.004$ ,  $\mu = 10$  and  $\gamma = 10 + 15i$ .

By denoting  $A = u + iv$ , we can decompose the equation into real and imaginary components, resulting in the following system of PDEs,

$$\begin{aligned} \frac{\partial u}{\partial t} &= \epsilon \Delta u + \mu(u - (u - 1.5v)(u^2 + v^2)), \\ \frac{\partial v}{\partial t} &= \epsilon \Delta v + \mu(v - (v + 1.5u)(u^2 + v^2)). \end{aligned}$$

Given the coupled dynamics of  $u$  and  $v$ , we present the relative  $L^2$  error of  $u$  in Table 1.

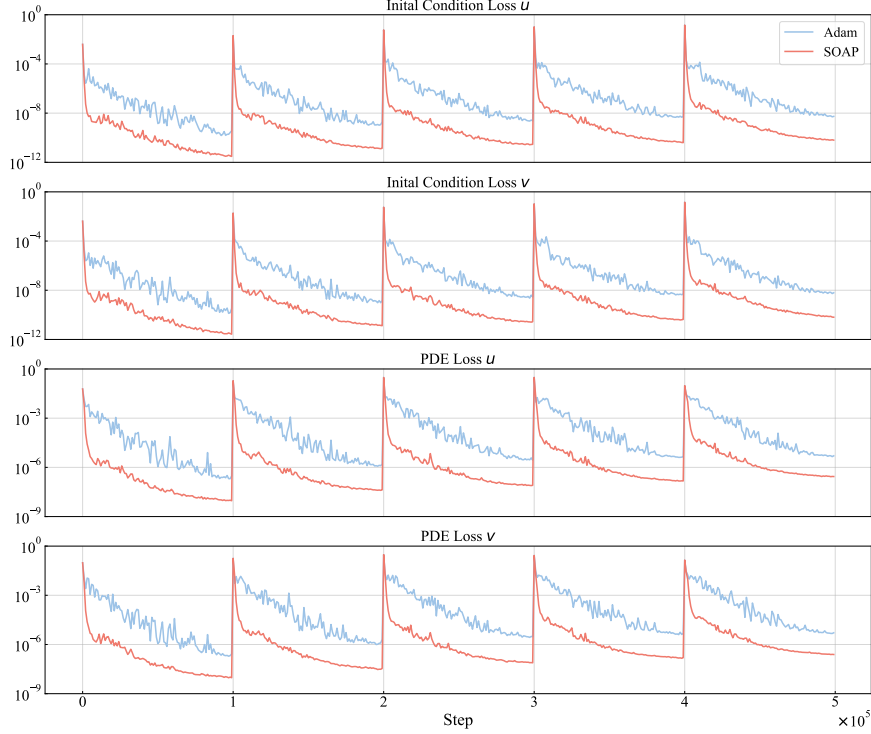


Figure 15: *Ginzburg-Landau equation*. Training loss trajectories for the Adam and SOAP optimizers.

**Lid-driven Cavity.** We study the incompressible Navier-Stokes equations in non-dimensional form for a two-dimensional domain:

$$\begin{aligned} \mathbf{u} \cdot \nabla \mathbf{u} + \nabla p - \frac{1}{Re} \Delta \mathbf{u} &= 0, \quad (x, y) \in (0, 1)^2, \\ \nabla \cdot \mathbf{u} &= 0, \quad (x, y) \in (0, 1)^2, \end{aligned}$$

where  $\mathbf{u} = (u, v)$  represents the steady-state velocity field,  $p$  is the pressure field, and  $Re$  is the Reynolds number which characterizes the ratio of inertial to viscous forces. This system models the equilibrium state of the flow, which is driven by the top boundary moving at a constant velocity while the other walls are stationary, leading to the formation of characteristic vortical structures whose complexity increases with the Reynolds number.

To ensure continuity at the corner boundaries, we implement a smoothed top-lid boundary condition:

$$u(x, y) = 1 - \frac{\cosh(C_0(x - 0.5))}{\cosh(0.5C_0)}, \quad v(x, y) = 0, \quad (\text{F.29})$$

where  $x \in [0, 1]$ ,  $y = 1$ ,  $C_0 = 50$ . For the other three walls, we enforce a no-slip boundary condition. Our goal is to obtain the velocity and pressure field corresponding to a Reynolds number of 5,000. The accuracy of our method is evaluated using the velocity magnitude  $\sqrt{u^2 + v^2}$ , with results presented in Table 1.

**Kolmogorov flow.** We study the two-dimensional Kolmogorov flow governed by the incompressible Navier-Stokes equations:

$$\begin{aligned} \mathbf{u}_t + \mathbf{u} \cdot \nabla \mathbf{u} &= -\nabla p + \frac{1}{Re} \Delta \mathbf{u} + \mathbf{f}, \\ \nabla \cdot \mathbf{u} &= 0, \end{aligned}$$

on the unit square domain  $(x, y) \in [0, 1]^2$ .

Here  $\mathbf{u} = (u, v)$  represents the time-varying velocity field, and  $\mathbf{f}$  denotes the external forcing term that maintains the flow structure. The system evolves from a random initial state and develops characteristic flow patterns, where energy transfers between different spatial scales through nonlinear interactions and viscous dissipation.

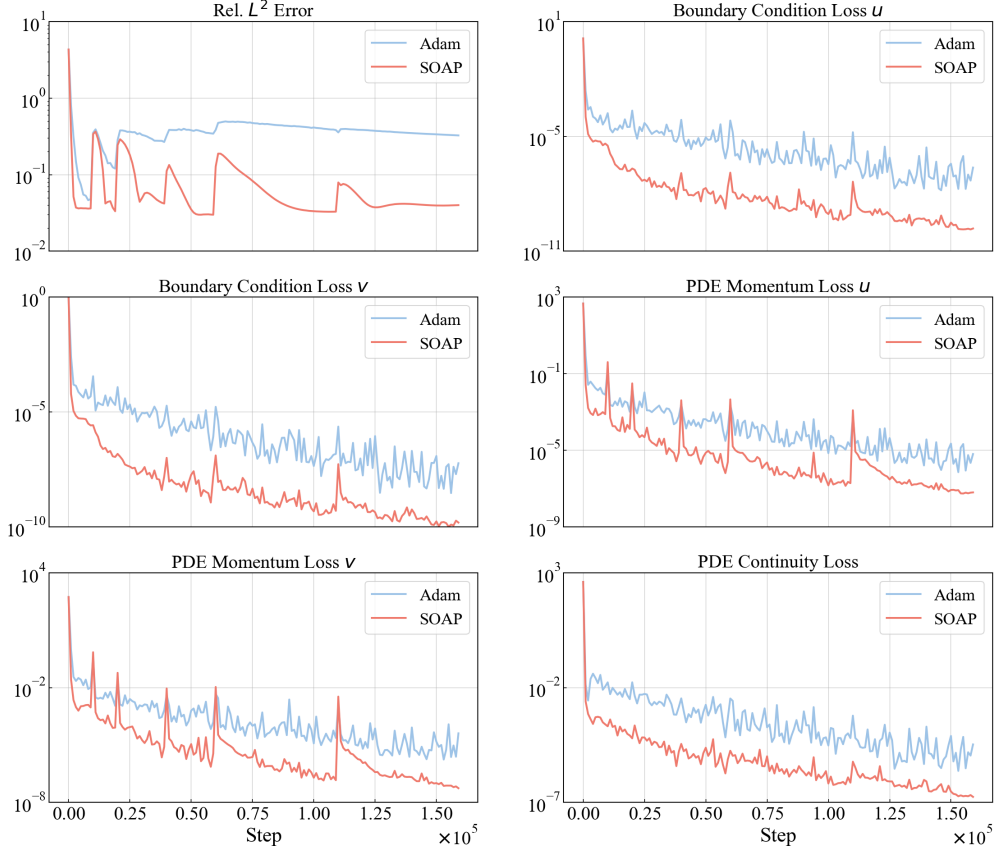


Figure 16: *Lid-driven Cavity*. Training loss and test error trajectories for the Adam and SOAP optimizers.

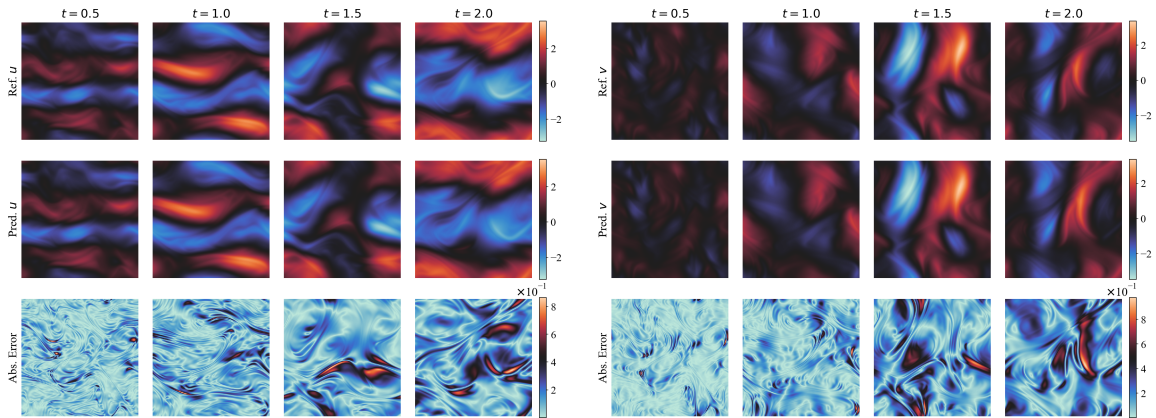


Figure 17: *Kolmogorov flow*. Comparison between reference solution and model predictions.

For our study, the system is driven by a sinusoidal forcing  $\mathbf{f} = (2 \sin(4\pi y), 0)$ . The numerical experiment initializes with a random initial condition and evolves until  $T = 2$ . The model's performance is quantified by the relative  $L^2$  error of vorticity (Table 1).

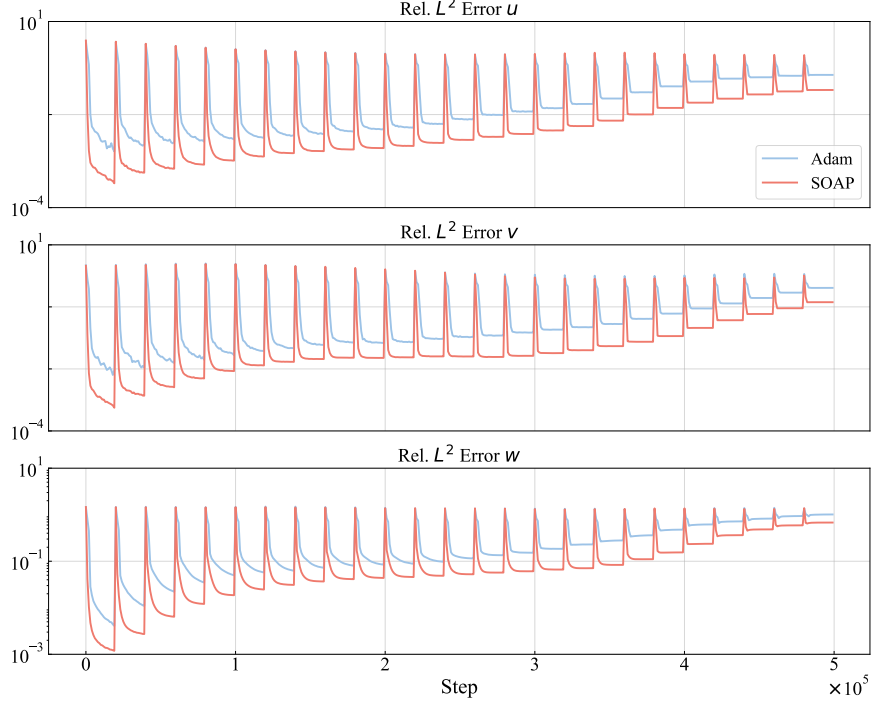


Figure 18: *Kolmogorov flow*. Test error trajectories for the Adam and SOAP optimizers.

**Rayleigh-Taylor instability.** We investigate a coupled flow-temperature system that models buoyancy-driven instability in a rectangular domain  $(x, y) \in [0, 1] \times [0, 2]$ :

$$\mathbf{u}_t + \mathbf{u} \cdot \nabla \mathbf{u} = -\nabla p + \sqrt{\frac{Pr}{Ra}} \Delta \mathbf{u} + T \mathbf{e}_y, \quad (\text{F.30})$$

$$\nabla \cdot \mathbf{u} = 0, \quad (\text{F.31})$$

$$T_t + \nabla \cdot (\mathbf{u}T) = \frac{1}{\sqrt{PrRa}} T_{tt} \quad (\text{F.32})$$

where  $T$  is the temperature field (acting as a density proxy through the Boussinesq approximation),  $Pr$  is the Prandtl number (ratio of momentum to thermal diffusivity), and  $Ra$  is the Rayleigh number (measuring buoyancy-driven flow strength). This system captures the characteristic mushroom-shaped plumes that develop as the heavier fluid penetrates into the lighter fluid below.

We set the Prandtl number  $Pr = 0.71$  and Rayleigh number  $Ra = 10^6$ . The boundary conditions are periodic in the horizontal direction for both  $\mathbf{u}$  and  $T$ , with Dirichlet conditions  $\mathbf{u} = T = 0$  imposed on the top and bottom boundaries. The accuracy of our method is evaluated using the temperature field, with results presented in Table 1.

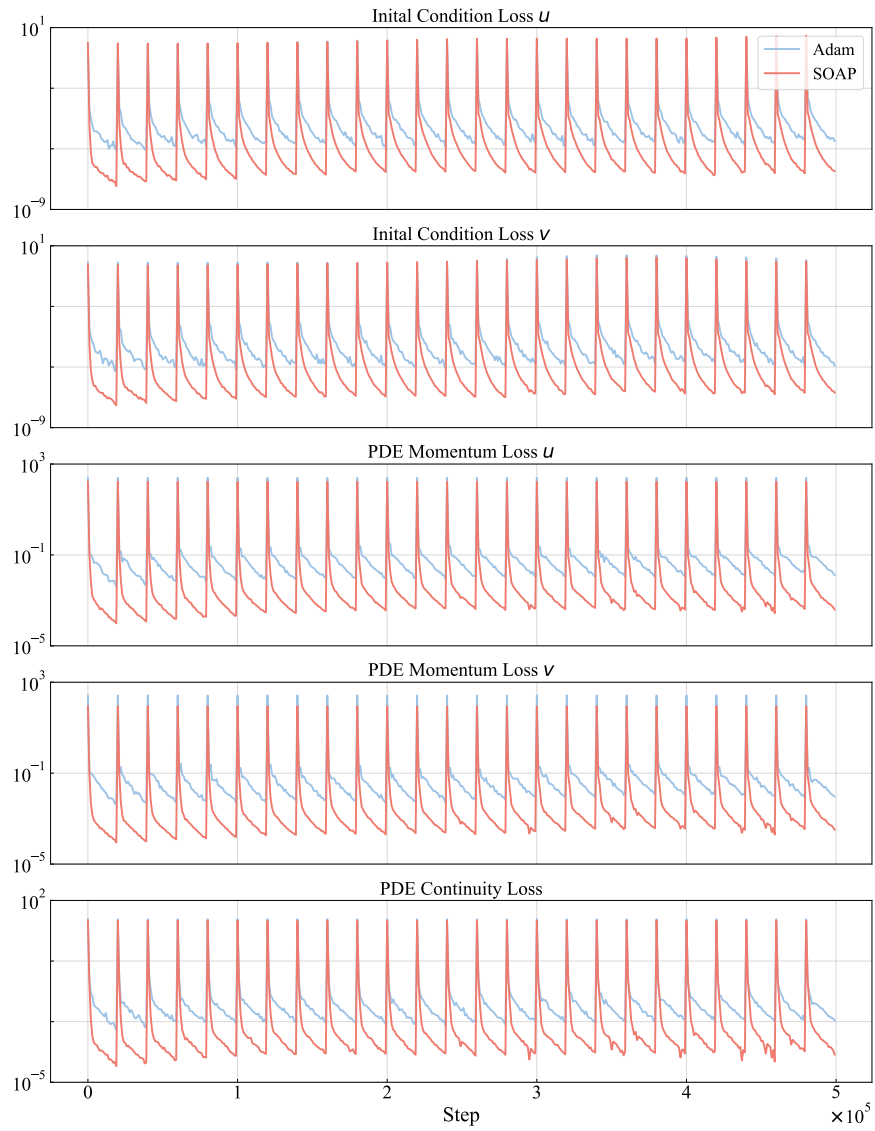


Figure 19: *Kolmogorov flow*. Training loss trajectories for the Adam and SOAP optimizers.

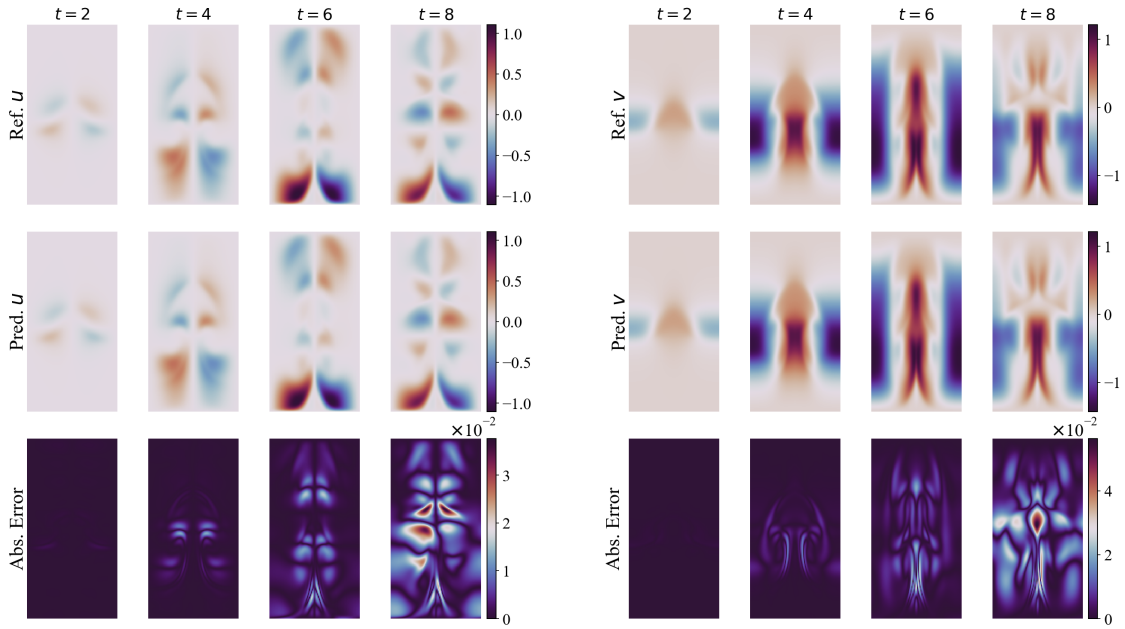


Figure 20: *Rayleigh-Taylor instability*. Comparison between reference solution and model predictions.

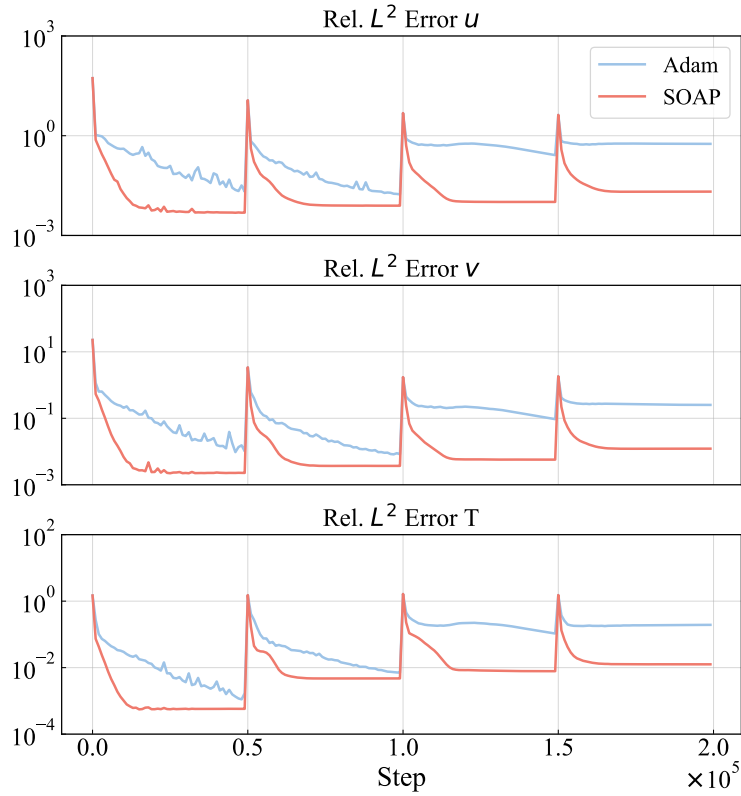


Figure 21: *Rayleigh-Taylor instability*. Test error trajectories for the Adam and SOAP optimizers.

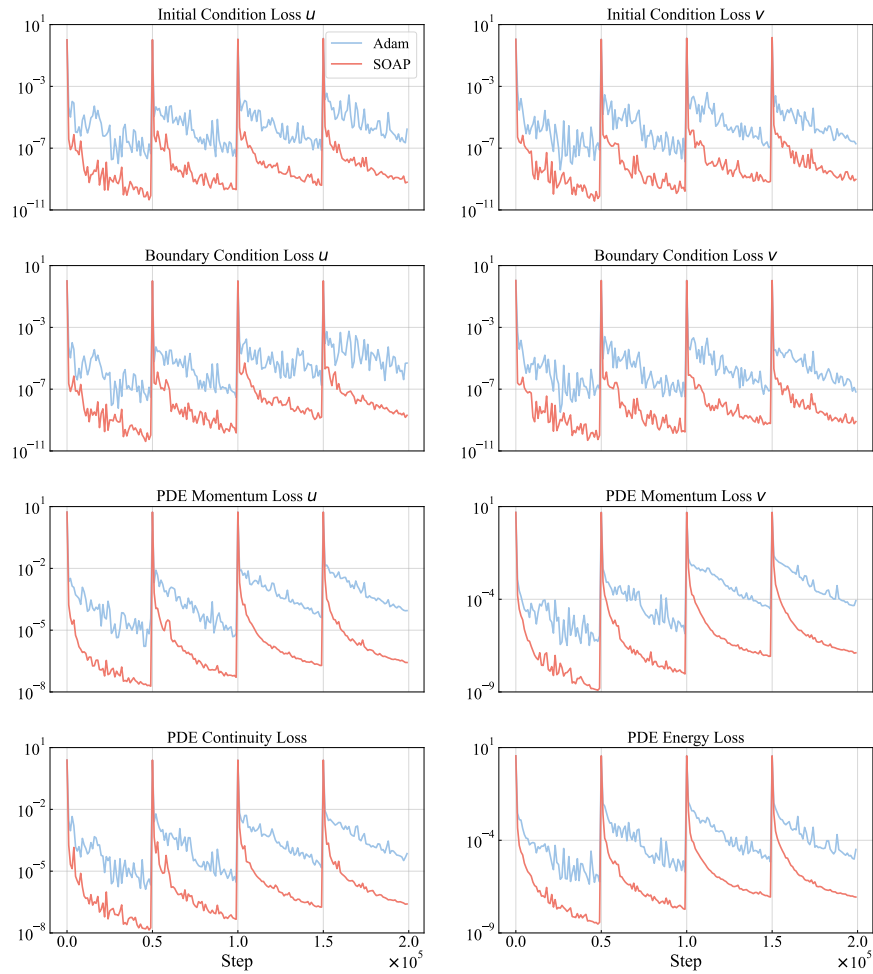


Figure 22: *Rayleigh-Taylor instability*. Training loss trajectories for the Adam and SOAP optimizers.